

**CHARACTERIZATION OF INKJET PRINTED HIGH NITROGEN
ENERGETIC MATERIALS AND BILAYER NANOTHERMITE**

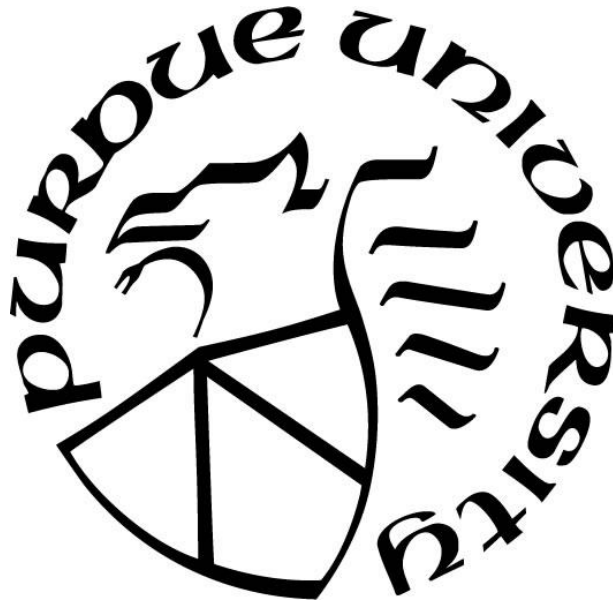
by
Adarsh Patra

A Thesis

Submitted to the Faculty of Purdue University

In Partial Fulfillment of the Requirements for the degree of

Master of Science in Aeronautics and Astronautics



School of Aeronautics & Astronautics

West Lafayette, Indiana

August 2019

**THE PURDUE UNIVERSITY GRADUATE SCHOOL
STATEMENT OF COMMITTEE APPROVAL**

Dr. Steven F. Son, Chair

Department of Mechanical Engineering

Dr. Jeffrey F. Rhoads

Department of Mechanical Engineering

Dr. I. Emre Gunduz

Department of Mechanical and Aerospace Engineering, Naval Postgraduate
School

Approved by:

Dr. Wayne Chen

Head of the Graduate Program

Dedicated to my family and friends for their lifelong support

ACKNOWLEDGMENTS

This research is supported by the U.S. Department of Defense, Defense Threat Reduction Agency through grant No. HDTRA1-15-1-0010 and is managed by Dr. Allen Dalton. The content of the information does not necessarily reflect the position or the policy of the U.S. federal government, and no official endorsement should be inferred. This material is also based upon work supported by the National Science Foundation Graduate Research Fellowship Program under Grant No. DGE-1842166. Any opinions, findings, and conclusions or recommendations expressed in this material are those of the author and do not necessarily reflect the views of the National Science Foundation.

I'd like to acknowledge my committee members, Professors Steven Son, Jeffrey Rhoads, and Emre Gunduz for their guidance in completing my research. I'd also like to thank fellow graduate students Miranda McConnell, Allison Murray, Trevor Fleck, and Forrest Son for their invaluable help with printing and testing. Additionally, I'd like to thank research scientist Tim Manship for helping with experiment setups and transporting energetic materials between labs several times.

TABLE OF CONTENTS

LIST OF TABLES	7
LIST OF FIGURES	8
ABSTRACT	10
1. INTRODUCTION	11
1.1 Project Motivation and Scope	11
1.1.1 Motivation.....	11
1.1.2 Project Scope	12
1.2 Background on Nanothermites	12
1.2.1 Nanothermite Combustion Properties.....	12
1.2.1.1 Methods of Tailoring Nanothermite Performance.....	13
1.2.2 Inkjet Printing of Nanothermites	16
1.3 Background on High Nitrogen Energetic Materials	19
1.3.1 Application to Inkjet Printing	21
2. DUAL-NOZZLE INKJET PRINTING OF BILAYER ALUMINUM BISMUTH OXIDE (III) NANOTHERMITE	22
2.1 Introduction.....	22
2.2 Materials and Methods.....	23
2.2.1 Ink Formulation	23
2.2.2 Dual-Nozzle Printing.....	24
2.2.2.1 Determining Printer Settings	25
2.2.3 Burning Rate Measurements.....	27
2.3 Results and Discussion	28
3. INKJET PRINTING OF HIGH NITROGEN ENERGETIC MATERIALS	31
3.1 Introduction.....	31
3.2 Materials and Methods.....	31
3.2.1 Ink Formulation	31
3.2.2 Inkjet Printing	32
3.2.3 Thermal Stability Analysis	33
3.2.4 Burning Rate Measurements.....	34

3.2.5	Closed Pressure Bomb Experiments.....	35
3.2.6	Microthruster Experiments	37
3.3	Results and Discussion	40
3.3.1	Ink Formulation Results	40
3.3.2	DSC/TGA Results	45
3.3.3	Burning Rate Results	48
3.3.4	Parr Cell Results	52
3.3.4.1	Experimental Results	52
3.3.4.2	Thermochemistry Calculations.....	54
3.3.5	Microthruster Results.....	57
4.	CONCLUSION.....	63
	REFERENCES	66

LIST OF TABLES

Table 1.1 Combustion reaction properties of common nanothermites [5]	13
Table 1.2 Propulsion performance of varying formulations and preparation methods of Al-CuO nanothermite in SPM configuration [6]	14
Table 1.3 Comparison of high nitrogen material sensitivities versus conventional propellant ingredients [20]	21
Table 3.1 Summary of thermal stability results at a heating rate of 10 °C/min	48
Table 3.2 Summary of microthruster performance results	60

LIST OF FIGURES

Figure 1.1 Experimental performance of an Al-CuO fueled SPM versus theoretical performance calculated with CEA [6].....	14
Figure 1.2 The effect of AP inclusion in an Al/CuO/NC (2.5 wt%) nanothermite formulation on important combustion parameters [7]	15
Figure 1.3 The effect of bulk density on combustion performance for an SPM fueled by Al-Bi ₂ O ₃ (2.5 wt% NC) [4]	16
Figure 1.4 Schematic of the PipeJet P9 piezoelectric inkjet printer system and printer head [12]	17
Figure 1.5 The results of burning rate study on printed Al-Bi ₂ O ₃ nanothermite versus the stoichiometric ratio used for ink preparation [13]	18
Figure 1.6 Molecular structure of BTATz and DAATO _{3.5} [19]	20
Figure 2.1 A diagram of a bilayer Al-Bi ₂ O ₃ nanothermite sample with the bilayer thickness labeled	22
Figure 2.2 Inkjet printing system in dual-nozzle configuration depositing a bilayer sample.....	25
Figure 2.3 Dimensions of dried nAl and nBi ₂ O ₃ samples versus printer pixel pitch.....	26
Figure 2.4 Microscopic images of dried nAl samples printed using different pixel pitches	26
Figure 2.5 Typical experimental set-up used for burning rate measurements	27
Figure 2.6 Images from a burning rate video of a 1.0 mm offset bilayer sample showing the propagation of the flame front	28
Figure 2.7 Al-Bi ₂ O ₃ nanothermite bilayer sample burning rates versus offset distance	29
Figure 3.1 Inkjet printing system depositing BTATz-DMF-PVP ink	33
Figure 3.2 Experimental set-up used for burning rate measurements	34
Figure 3.3 Sticker samples drying with varying amounts of deposited BTATz ink.....	35
Figure 3.4 Parr cell experimental setup	37
Figure 3.5 Dimensioned CAD renderings of microthruster components in millimeters	38
Figure 3.6 Experimental setup used to acquire thrust force traces of microthruster samples	39
Figure 3.7 (a) CAD rendering of microthruster array and (b) 3D printed array loaded with wet BTATz ink	40
Figure 3.8 Recrystallized BTATz using DMF as the solvent.....	41
Figure 3.9 Recrystallized BTATz using DMSO as the solvent.....	42

Figure 3.10 Dried BTATz deposited as a suspension with n-hexane	43
Figure 3.11 Microscopic image of an inkjet printed BTATz sample on Novele substrate	44
Figure 3.12 Microscopic image of an inkjet printed DAATO _{3.5} sample on Novele substrate.....	45
Figure 3.13 DSC results comparing two BTATz ink samples at different heating rates.....	46
Figure 3.14 DSC/TGA data for (a) BTATz and (b) DAATO _{3.5} inks at a heating rate of 10 °C/min	47
Figure 3.15 Burning rate of BTATz ink at varying binder inclusion levels and layers.....	49
Figure 3.16 Confined versus unconfined printed BTATz burning rates	50
Figure 3.17 High-speed images of burning (a) unconfined and (b) unconfined BTATz samples	50
Figure 3.18 Comparison of DAATO _{3.5} and BTATz ink burning rates.....	51
Figure 3.19 Comparison of dynamic pressure traces for (a) BTATz ink and (b) DAATO _{3.5} ink	53
Figure 3.20 Comparison of peak static pressures generated by BTATz and DAATO _{3.5} samples	54
Figure 3.21 Comparison of pressurization rates for (a) BTATz ink and (b) DAATO _{3.5} ink.....	54
Figure 3.22 Predicted peak pressures determined using CHEETAH simulations.....	56
Figure 3.23 Theoretical pressures calculated using simplified thermochemistry model.....	57
Figure 3.24 Thrust traces for samples filled with 200 μL of (a) BTATz and (b) DAATO _{3.5} ink.	58
Figure 3.25 High-speed images showing ignition of a microthruster loaded with BTATz ink....	59
Figure 3.26 High-speed images showing ignition of a microthruster loaded with DAATO _{3.5} ink	59
Figure 3.27 High-speed schlieren images of a microthruster array ignition test	62

ABSTRACT

Author: Patra, Adarsh, MSAAE

Institution: Purdue University

Degree Received: August 2019

Title: Characterization of Inkjet Printed High Nitrogen Energetic Materials and Bilayer Nanothermite

Committee Chair: Steven F. Son

This thesis presents work on two major areas of research. The first area of research involves the use of a dual-nozzle piezoelectric inkjet printing system to print bilayer aluminum bismuth (III) oxide nanothermite samples. The combinatorial printing method allows for separate fuel and oxidizer inks to be printed adjacent to each other at prescribed offset distances. The effect of the bilayer thickness on the burning rate of the samples is investigated using high-speed imaging. Analysis of the burning rate data revealed that there is no statistically significant relationship between these two parameters. This result was used to determine the dominant processes that control the propagation rate in nanothermite systems. It was concluded that convective processes dominate the burning rate rather than diffusive processes. The second area of research involved synthesizing inks suitable for inkjet printing using two promising high nitrogen energetic materials called BTATz and DAATO_{3.5}. The performance of the developed inks was characterized using four experiments. The thermal stability and exothermic behavior of the inks were determined using DSC and TGA analysis. The results revealed that the inks are more thermally stable than the base materials. The inks were used to print lines that were subsequently used to determine burning rates. DAATO_{3.5} samples were determined to have faster burning rates than BTATz. Closed pressure bomb experiments were conducted to determine the gas producing capability of the high nitrogen inks. BTATz samples showed better performance in terms of peak static pressures and pressurization rates. 3D printed microthrusters were developed to test the thrust performance of the inks. Peak thrust, total impulse, and specific impulse values are reported and were determined to be suitable for use with Class 1 micro-spacecraft. Finally, a microthruster array prototype was developed to demonstrate the capability to use additive manufacturing to create high packing density arrays.

1. INTRODUCTION

1.1 Project Motivation and Scope

1.1.1 Motivation

Currently, there exists a pressing need to secure and control access to high-valued electronics and microelectromechanical systems (MEMS) or complementary metal-oxide-semiconductor (CMOS) devices such as those critical to the Department of Defense (DOD) systems. This need is becoming more important with the advancement of electronic warfare threats which could potentially compromise DOD systems. The Defense Threat Reduction Agency (DTRA) has called for the development of SecureMEMS to meet this need. In this context, SecureMEMS are MEMS or CMOS devices with the ability to be rendered safe or inoperable from a sufficient stand-off distance. Thus, there is now significant interest in developing SecureMEMS and one promising method is the integration of energetic materials (EMs) with MEMS or CMOS devices using selective deposition.

EMs store large amounts of the chemical since they generally are comprised of fuel and oxidizer. This type of material transfers its chemical energy to kinetic and thermal energy once combustion is initiated. EMs are commonly classified in three categories; propellants, explosives, and pyrotechnics. Each type of energetic material has an array of applications and each is commonly utilized for both civil and military applications [1]. For example, propellants can be used for a variety of propulsion needs such as rocket propulsion or gas-powered actuators [2]. Pyrotechnics are used for fireworks, military flares, and even mining or quarrying. Thus, the integration of EMs with electronics has several interesting potential applications in addition to SecureMEMS. Potential applications include microthrusters, airbag inflation initiators, and even emergency drug delivery systems. Since there are a vast number of EMs with a variety of applications, incorporating them into AM methods presents a unique opportunity. The precision of modern AM technologies promises the ability to tailor the functional performance of EMs through multiple parameters.

There are several fundamental questions that need to be answered before the integration of EMs can be reliably used in SecureMEMS and other applications. The first question is what EMs are suitable or compatible for direct use with these devices? Next is the question of how material parameters influence the final reactive or mechanical properties of the selectively-deposited materials. Then the question becomes how much energy is necessary to initiate the combustion reaction of the deposited energetic material. In the case of SecureMEMS, the final fundamental question is whether the selectively deposited energetic material can successfully disable critical MEMS or CMOS components?

1.1.2 Project Scope

There have been several recent advancements in AM methods that utilize EMs such as inkjet printing of EMs. The work presented in this thesis aims to further the capabilities of selective deposition of EMs and characterize the performance of relatively new EMs. The scope of this thesis is focused on two major areas. The first focus is on tailoring the performance of inkjet printed nanothermite using a dual nozzle printing configuration. The second focus is on developing fundamental knowledge on a relatively new class of EMs called high nitrogen (HN) materials and exploring its use in inkjet printing. This part of the work also characterizes the performance of HN inks in various configurations to demonstrate their feasibility for use in some potential applications, such as gas actuators and microthrusters.

1.2 Background on Nanothermites

1.2.1 Nanothermite Combustion Properties

Nanothermites are a type of metastable intermolecular composite (MIC) that is comprised of metal and metal oxide powders with nano-sized particles. This MIC is known for its quick and highly exothermic reactions that are a result of minuscule diffusion scales. In general, nano-EMs are known to have better performance over traditional EMs in terms of ignition energy, burning rates, and brisance [3]. The enhanced performance is explained by high specific surface area which means there are more surface atoms per mass compared to conventional materials. The high specific surface area contributes to faster heat release and lower activation thresholds [3]. The burning rates of nanothermites are adaptable through preparation methods; speeds ranging from 0.03 to 2600 m/s have been demonstrated [4]. This adaptability translates to tunable performance

which makes this material particularly interesting because it enables optimization for specific applications.

There are several formulations of nanothermites; however, some are better suited for certain application than others. Aluminum bismuth oxide (III) nanothermite (Al-Bi₂O₃) is relatively dense, has a fast combustion wave speed and high combustion gas generation. Aluminum cupric (II) oxide nanothermite (Al-CuO) is also of interest because of its fast propagation rate, high volumetric impulse, density and heat of reaction [5]. Combustion characteristics and material properties, such as theoretical maximum density (ρ_{TMD}), of several common nanothermites are summarized in Table 1.1.

Table 1.1 Combustion reaction properties of common nanothermites [5]

Reactants		Adiabatic temperature	Gas production	Heat of reaction	
Constituents	ρ_{TMD} (g/cm ³)	phase change (°C)	per gram	Q (cal/g)	Q (cal/cm ³)
2Al + Bi ₂ O ₃	7.188	2979	0.8941	506.1	3638
8Al + Co ₃ O ₄	4.716	2928	0.1294	1012	4772
2Al + 3CuO	5.109	2570	0.3421	974.1	4976
2Al + Fe ₂ O ₃	4.175	2862	0.0784	945.4	3947
2Al + MoO ₃	3.808	2980	0.2473	1124	4279

1.2.1.1 Methods of Tailoring Nanothermite Performance

Previous work has shown that the performance of nanothermite as a propellant can be modulated by additives such as nitrocellulose (NC). Additionally, nanothermites have been paired with other conventional propellants to create composites that tend to perform better in solid propellant microthruster (SPM) configurations. In these composites, nanothermites provide fast energy release as a heat source and the conventional propellants provide the gas generation resulting in improved performance. The preparation method can also influence the performance of nanothermites as shown by Ru's research group [6]. In their study, two methods of the assembly were used to create mesoparticles of Al-CuO thermite; electrospray (ES) and mechanical mixing (MM). They found that the propulsion metrics of total impulse and specific impulse increased with increasing mass content of NC when using the ES method. However, for the MM method, the total

impulse and specific impulse peaks with 2.5 wt% NC and drops off at 5 wt% NC [6]. These results are summarized in Table 1.2. It is important to note that increasing NC content consequently increases diffusion lengths within the MIC and reduces the reaction rate [4]. Additionally, ES is known to be more effective at mixing composites than MM. This is clearly shown in the 10 wt% NC formulation where the MM composite did not ignite but the ES one did.

Table 1.2 Propulsion performance of varying formulations and preparation methods of Al-CuO nanothermite in SPM configuration [6]

Propellant	Total impulse, $\mu\text{N}\cdot\text{s}$	Average thrust, N	Specific impulse, s
Al/CuO (MM)	155.9 ± 44.9	0.479	10.2 ± 3.3
Al/CuO/NC (2.5 wt%, MM)	225.2 ± 31.8	0.574	17.7 ± 2.5
Al/CuO/NC (5.0 wt%, MM)	186.6 ± 56.2	0.500	14.6 ± 4.4
Al/CuO/NC (10.0 wt%, MM)	–	–	–
Al/CuO/NC (2.5 wt%, ES)	218.0 ± 33.8	0.495	17.1 ± 2.7
Al/CuO/NC (5.0 wt%, ES)	309.6 ± 44.9	0.645	24.3 ± 3.5
Al/CuO/NC (10.0 wt%, ES)	346.9 ± 56.2	0.605	27.2 ± 4.4

As shown in Figure 1.1, it is difficult to experimentally match the theoretical performance that thermochemistry codes such as NASA's Chemical Equilibrium Application (CEA) predict. This is due to the several ideal assumptions that are made in these codes like adiabatic, isentropic expansion, complete mixing, and combustion [6].

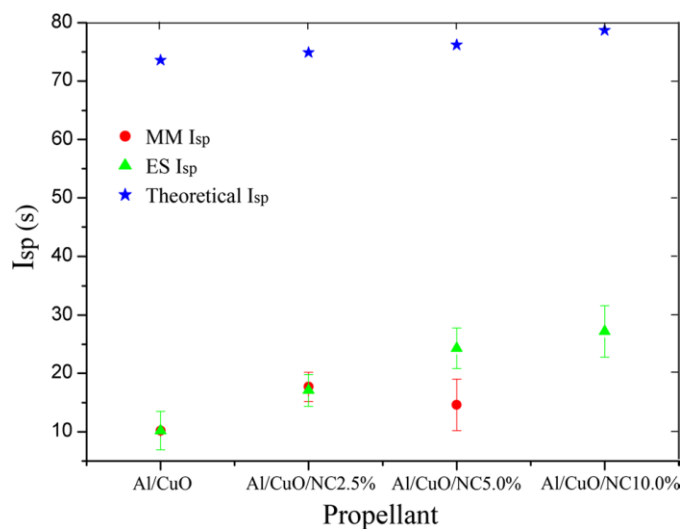


Figure 1.1 Experimental performance of an Al-CuO fueled SPM versus theoretical performance calculated with CEA [6]

Recently, Ru's group also investigated the effect of adding ammonium perchlorate (AP) to the Al/CuO/NC (2.5 wt%) formulation. AP is conventionally used in solid propellant rocket engines due to its high burning rate and gas producing properties. In this study, AP was used as an additive to modulate the performance of the original ES deposited nanothermite-based propellant within the same type of SPM system as in the NC inclusion study. Overall, the inclusion of AP seemed to improve critical performance parameters like heat release, specific impulse, and chamber pressures. The 7.5 wt% AP formulation demonstrated a ~270% increase in specific impulse and ~140% increase in heat release (compared to the original formulation) in thrust experiments. Additionally, the ignition delay times were comparable to the original Al/CuO/NC. A holistic analysis of the effect of AP on combustion performance is shown in Figure 1.2.

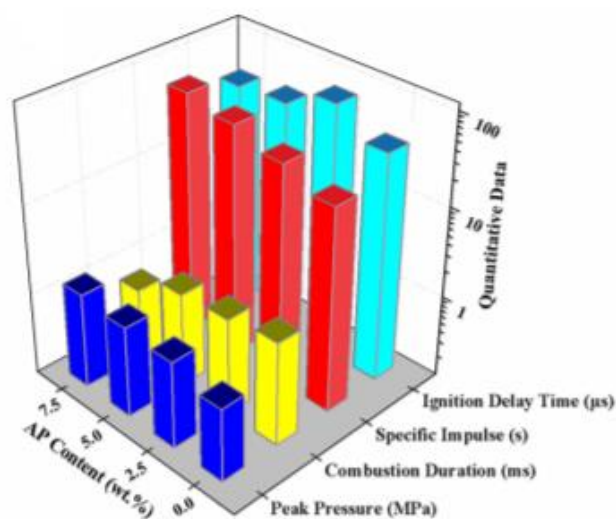


Figure 1.2 The effect of AP inclusion in an Al/CuO/NC (2.5 wt%) nanothermite formulation on important combustion parameters [7]

Another important factor that determines how nanothermites will perform in a microchamber is the packing density. Staley's group investigated this relationship for Al-Bi₂O₃ nanothermite [4]. Two regimes of reaction rates for these MICs have been shown. When the packing density is low enough, convective processes dominate, and combustion is rapid. However, when sufficient density is achieved, the reaction rate is significantly slower presumably due to diffusive, conductive mechanisms that control the propagation rate. This transition occurs when the density

increases to a point where there aren't enough voids with air pockets to sustain convective heat transfer [4]. This relationship is quantified for a formulation of Al-Bi₂O₃ with 2.5 wt% NC for varying bulk densities from 25 to 65% of TMD in Figure 1.3. Thrust forces for low-density tests were found to be an order of magnitude higher than those of high-density tests.

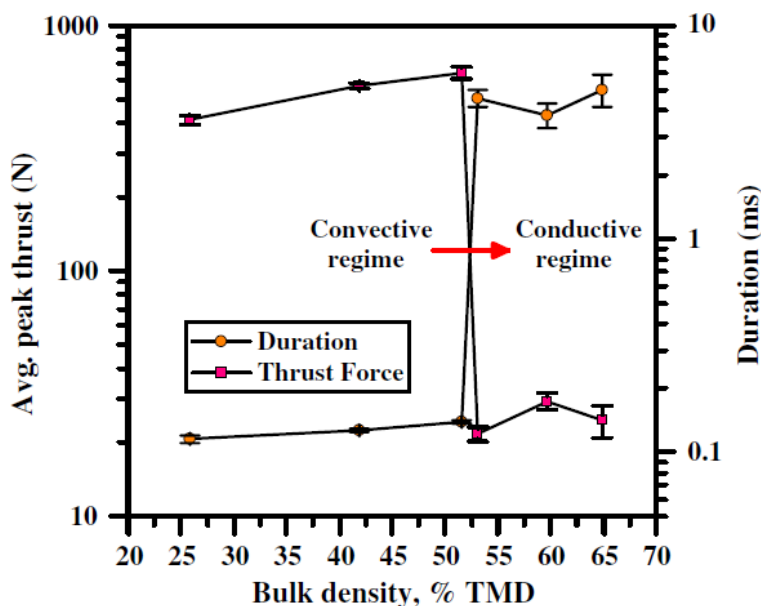


Figure 1.3 The effect of bulk density on combustion performance for an SPM fueled by Al-Bi₂O₃ (2.5 wt% NC) [4]

1.2.2 Inkjet Printing of Nanothermites

In recent years, there have been substantial advances in the field of inkjet printing of nanoEMs. When integrating EMs with MEMS and other electronic devices, there are few viable safe methods. Traditional methods for deposition include electrophoresis, doctor blading, and inkjet printing [8]. Inkjet printing is advantageous because it is an additive technique better suited for precise deposition of small volumes with micron resolution. Virtually any material can be printed using this method if it can be formulated into a low-viscosity ink [9]. However, there are several compatibility challenges when using nanoparticles in inkjet materials. These challenges include agglomeration, solids loading, and ink homogeneity. Several recent studies have addressed these issues and have optimized the formulation of nanothermite inks use with inkjet printing [9],[10],[11]. There are several types of inkjet printing; however, for this application, piezoelectric

inkjet printing is the most promising. Piezoelectric inkjet printing allows for flexibility in the types of inks used because it actuates the nozzle via a change in the shape of a piezoelectric material. This means that the method of producing ink droplets doesn't rely on thermally affecting the ink which is considerably safer when dealing with energetic inks that are potentially thermally sensitive.

Recent studies have been published that utilize a custom-built piezoelectric printer as an experimental platform and proving ground for the inkjet printing of EMs. This printing system can use multiple types of piezoelectric printing heads; however, previous studies concluded that the PipeJet P9 system is best suited for energetic inks [12]. Thus, this system was used for all of the printing procedures for the work presented in this thesis. A schematic of the printing system is shown in Figure 1.4.

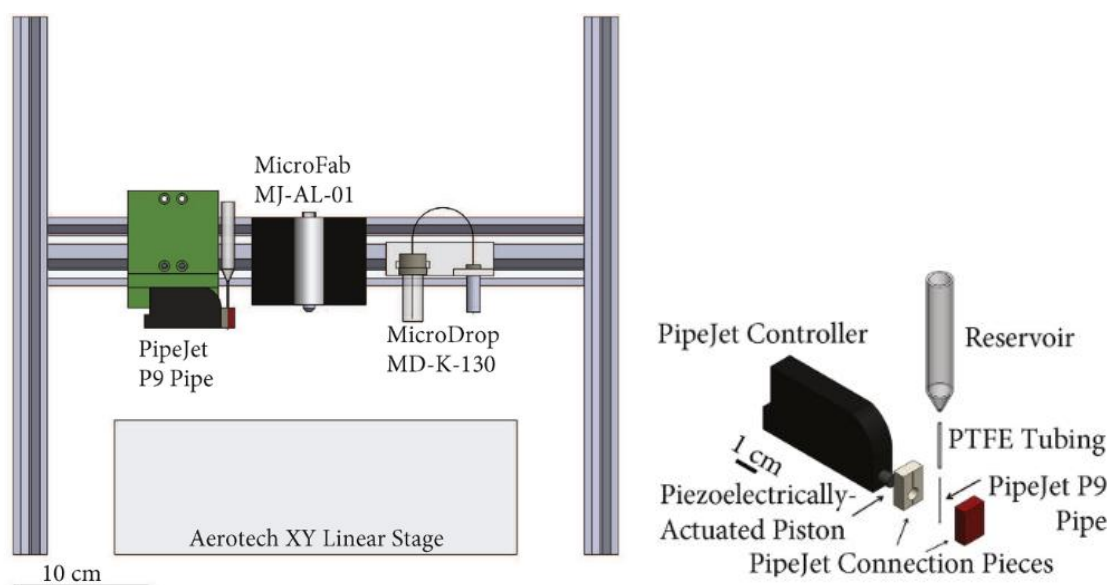


Figure 1.4 Schematic of the PipeJet P9 piezoelectric inkjet printer system and printer head [12]

Several studies on inkjet printed nanothermite have been conducted using this system with the aim of characterizing the effect of variables on the final performance of the deposited EMs. One recent study analyzed how the stoichiometry at which Al-Bi₂O₃ and Al-CuO inks were prepared affected the destructive capability and the burning rates of the printed nanothermite [13]. The results showed that an equivalence ratio of $\phi = 2$ resulted in the best performance for both destruction and burning rates [13]. Additionally, the study showed that Al-Bi₂O₃ nanothermite

consistently outperformed Al-CuO nanothermite in both measures. The effect of the equivalence ratio on the burning rate for printed Al-Bi₂O₃ is shown in Figure 1.5. Due to these results, Al-Bi₂O₃ nanothermite was used at an equivalence ratio of $\varphi = 2$ for the nanothermite related work presented in this thesis.

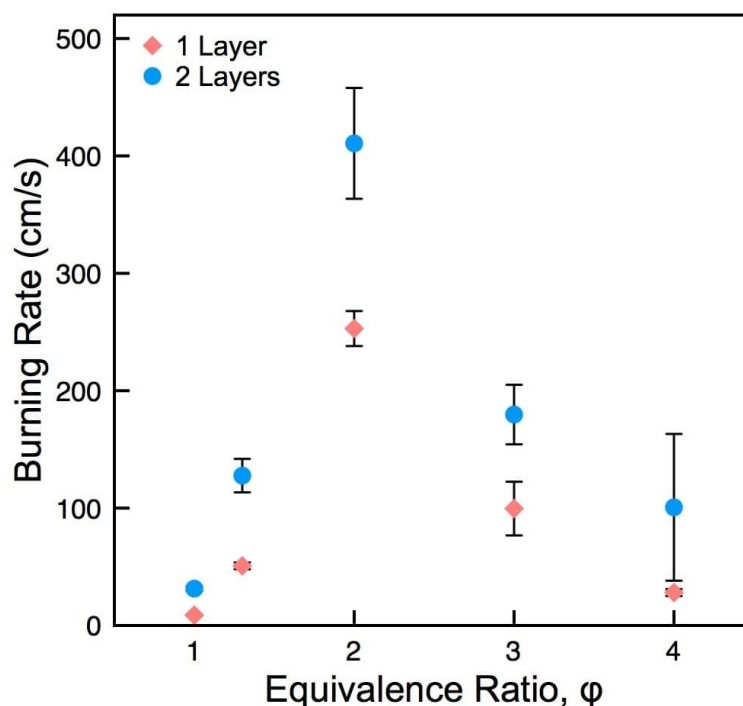


Figure 1.5 The results of burning rate study on printed Al-Bi₂O₃ nanothermite versus the stoichiometric ratio used for ink preparation [13]

Even more recently, additional studies have been conducted related to the printing parameters and sample geometry affect the performance of nanothermite. Another recent study focused on the combinatorial printing capability of the PipeJet printer where two piezoelectric actuators are used to print two separate inks side-by-side [8]. The study used two inert colloidal suspensions as the inks, one with nAl and one with nCuO. They were able to demonstrate in situ mixing to produce a nanothermite which is arguably a safer method than using premixed ink. They compared the performance of this dual-nozzle nanothermite against premixed nanothermite ink. The results showed that qualitatively, through scanning transmission electron microscopy (STEM) that the dual-nozzle samples were similarly mixed when enough material was deposited. However, the combustion performance was reduced compared to the premixed samples [8].

1.3 Background on High Nitrogen Energetic Materials

HN EMs are a relatively new class of EMs that are characterized by their high nitrogen compositions and are potentially high performing and insensitive. Since these materials are known to produce large amounts of gas when combusted, they have many potential applications including microthrusters, gas actuators, fire suppression systems, airbag inflation initiators, etc. HN EMs generally deflagrate without external oxidation and instead utilize their high positive heat of formations to release energy. These materials can be used as propellants since they are gas-generating and can achieve high theoretical specific impulse while maintaining low combustion temperatures. HN EMs have molecular structures that include tetrazine-based heterocyclic compounds that maximize nitrogen atoms in a stable ring. The inclusion of nitrogen atoms in these molecular structures greatly increases the enthalpy of formation due to the high N-N bond strengths. These impressive energy contents make these EMs capable of being explosive and exhibiting detonation velocities around and above 7500 m/s [14],[15]. Tetrazine rings are also known to have high stability with regards to thermal stimuli, most tetrazine derived compounds decompose around or above 300 °C [16]. Additionally, research has proven these materials to be insensitive to impact, electrostatic discharge (ESD) and friction [15].

Although s-tetrazines were discovered as far back as the nineteenth century, there have been many recent advances in derivatives of this molecule. Generally, these derivatives can be classified into four types; CHN-tetrazines, CHNO-tetrazines, tetrazine salts with oxidizing acids, and tetrazine salts with nitrates and perchlorates. Of all known CHN-tetrazines, 3,6-bis(1H-1,2,3,4-tetrazol-5-yl-amino)-s-tetrazine (BTATz) appears to be the best suited for solid propellant microthruster (SPM) and actuation applications. BTATz is known to be insensitive and exhibits a moderate pressure exponent which are all desirable properties for propellants [17]. The pressure exponent quantifies the relationship between chamber pressure and the burning rate of a propellant, lower values are desired as it results in stable thrust performance. Previous research has demonstrated that BTATz has fast burning rates that are tunable via binder inclusion or purification [18]. Additionally, the decomposition and exothermic behavior of BTATz have been studied by multiple groups and is relatively well understood [19].

Theoretically, CHNO-tetrazines should have improved energetic performance because of the inclusion of active oxygen in the molecule. Detonation velocities have been calculated for these materials and they are like that of cyclotrimethylene-trinitramine (RDX) or cyclotetramethylene-tetranitramine (HMX). One of the newest and most promising CHNO-tetrazines is a mixture of N-oxides and 3,3'-azobis(6-amino-1,2,4,5-tetrazine) (DAAT) is named DAATO_{3.5}, where the 3.5 subscript represents the average oxygen content. It has been reported that DAATO_{3.5}'s burning rate may be faster than that of all other known stable organic solids. Additionally, it has a desirable low pressure exponent making it well suited for application in SPM systems. Ali et al. demonstrated that DAATO_{3.5} is readily ignitable while still having relatively low sensitivity to various stimuli [20].

Of all of the relatively newly synthesized HN materials, BTATz and DAATO_{3.5} appear to be the most promising from their respective s-tetrazine subgroups for SPM and actuation applications. Both propellants are noncorrosive, shelf stable at ambient conditions and have environmentally benign combustion products [20]. Additionally, these materials have favorable thermal and vacuum stability as well as impact and friction sensitivities when compared to other conventional propellants. Ali et al. also showed that these sensitivities can be further reduced by inclusion of inert binders such as polyethyl acrylate (PEA) or polyvinyl alcohol (PVA) [20]. Thus, these two HN EMs were selected for use in this research. Both of their molecular structures can be seen in Figure 1.6 and

Table 1.3 compares their sensitivities to other commonly used EMs.

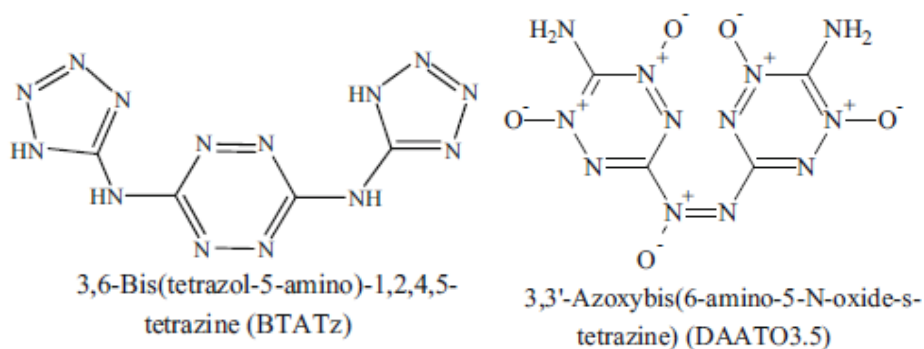


Figure 1.6 Molecular structure of BTATz and DAATO_{3.5} [19]

Table 1.3 Comparison of high nitrogen material sensitivities versus conventional propellant ingredients [20]

Material	Impact sensitivity H ₅₀ , kg · cm	DSC onset, °C	Friction sensitivity, kg	Vacuum stability (100°C)
Lead styphnate, normal	17 ^a	N/A	N/A	N/A
MMW-GAP	200 ^b	240 ^c	32.4 ^b	≥3 ml/g (uncured) ^b
Pure BTATz	80	264	>36	0.22 ml/g
BTATz/ 3% PEA	250	255	22	0.11 ml/g
Pure DAATO3.5	50	177	2–14	N/A
DAATO3.5/ 5% PVA/ 1%TEG	80	169	17.4	15.5 ml/g
PETN ^d	30–35	N/A	9	N/A
HMX	57.5	N/A	N/A	0.08 ml/g

1.3.1 Application to Inkjet Printing

To the best of the authors' knowledge, currently there is no published research on the use of HN EMs with inkjet printing systems. The ability to precisely and selectively deposit HN EM inks will provide a foundation to create high performing MEMS based devices for use in micropropulsion and actuation applications. The foci of this work are on formulations of feasible HN energetic inks for use with a piezoelectric inkjet printing system and characterization of the combustion performance of these inks in the context of the intended applications. The objective of this research is to demonstrate the feasibility of the use of HN EMs in these applications and lay the foundation for further studies on and how to tailor their performance.

2. DUAL-NOZZLE INKJET PRINTING OF BILAYER ALUMINUM BISMUTH OXIDE (III) NANOTHERMITE

2.1 Introduction

As discussed in the background section, there are many methods of tailoring the performance of nanothermite by changing formulation and mixing methods. When it comes to the inkjet printing of nanothermites, the effects of printing parameters and sample geometries have been investigated [13]. Additionally, the use of a dual-nozzle configuration has been used to investigate the performance of nanothermite mixed *in situ* [8]. This combinatorial printing capability enables research on the performance of bilayer nanothermite samples. A bilayer sample is simply two layers of nanothermite that are printed adjacently and in parallel with a prescribed distance between the two layers. Bilayer thickness refers to this distance between the centerlines of the two layers of constituent inks which are the fuel and oxidizer respectively. Figure 2.1 shows a diagram of what is meant by the bilayer thickness.

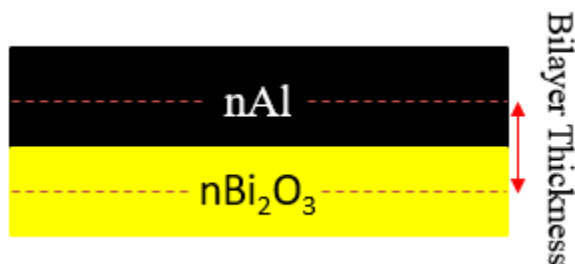


Figure 2.1 A diagram of a bilayer Al-Bi₂O₃ nanothermite sample with the bilayer thickness labeled

The nanothermite related work in this thesis attempts to answer a fundamental question about nanoenergetic combustion. One of these fundamental questions is the effect of bilayer thickness on propagation rates in nanoscale particle reactive systems, i.e. what are the mechanisms that control combustion in these systems [21]. It has been argued that diffusive processes dominate the propagation mode in thin film energetic systems, such as those comprised of nickel and aluminum foils [22]. The dual-nozzle printing configuration provides the ability to precisely control the bilayer thickness which defines the diffusion scale of the sample. Thus, using this method, the role of the diffusion scale on the propagation rate of nanothermites can be investigated. The overall

aim of this study is to elucidate the mode of propagation that controls combustion in nanothermite systems.

2.2 Materials and Methods

2.2.1 Ink Formulation

As mentioned previously, an equivalence ratio of two has been shown to have the best performance for Al-Bi₂O₃ nanothermite in terms of burning rate and destructive performance [13]. Thus, the separate fuel and oxidizer inks were prepared such that if equal volumes of each ink were mixed, the theoretical equivalence ratio would equal two. The equivalence ratio is defined by the following equation,

$$\varphi = \frac{\left(\frac{F}{A}\right)_{actual}}{\left(\frac{F}{A}\right)_{stoichiometric}}, \quad (2.1)$$

where F represents the number of moles of fuel and A represents the number of moles of oxidizer. The denominator of the equation represents the stoichiometric ratio of moles of fuel to moles of oxidizer. This ratio can be determined from the following chemical equation for the stoichiometric reaction for Al-Bi₂O₃ nanothermite.



Nanoparticles were mixed in a solvent with a surfactant to create the fuel and oxidizer inks following a procedure similar to that used in previous studies [8]. The aluminum nanoparticles (NovaCentrix, 80 nm, 79% active Al) were known to have passivated alumina (Al₂O₃) shells. The powder was stored in a positive pressure argon glovebox to prevent additional passivation. When the powder was needed, it was removed from the glovebox in vacuum sealed containers. The active content of the nanoparticles was accounted for in the equivalence ratio calculations to determine the required mass of the ink ingredients. The oxidizer ink was synthesized using bismuth oxide (III) nanoparticles (Alfa Aesar, 38 nm). The solvent used for both inks was N, N-dimethylformamide (DMF, Sigma-Aldrich, anhydrous, 99.8%). The surfactant that was mixed with the solvent was Solsperse 41000 (Lubrizol). This surfactant was used to improve the suspension and dispersion of the nanoparticles in the ink. A previous sedimentation study identified this surfactant to be effective with this nanothermite system [11]. This study also suggested that the ideal proportion of surfactant to include is 5% of the solids mass, thus that ratio

was used to prepare the solvent and surfactant mixture. For this study, a volumetric solids loading of 2% was used for the bismuth (III) oxide ink. As discussed previously, the aluminum ink was then prepared such that its solids loading would provide the desired equivalence ratio if one drop of an equal volume of each ink was mixed. The necessary masses or volumes for the ink constituents were calculated using a spreadsheet that considered densities, ratios, and other factors includes active aluminum content. Once the powders were weighed out, they were transferred into separate centrifuge tubes (VWR). Next, the proper amount of the DMF/Solsperse 41000 mixture was pipetted into each of the centrifuge tubes. The tubes were then closed and shaken by hand to dislodge any settled solids and then placed in an ultrasonic bath (Branson, Inc.) for 30 min directly prior to printing.

2.2.2 Dual-Nozzle Printing

In order to create repeatable bilayer samples, an inkjet printing system that has been used in previous studies to print nanothermite was used for this research [8], [12], [13]. The printing system was configured such that it used dual piezoelectric actuated Pipejet P9 (Biofluidix) printing heads. These print heads were fixed above a dual-axis linear positioning stage (Aerotech Planar DL 200-XY, 200 mm travel, 0.5 μm accuracy). 500 μm diameter P9 nozzles were attached to one end of approximately 2 cm long pieces of polytetrafluoroethylene (PTFE) tubing with an inner diameter of 1.6 mm. The other ends of the PTFE tubing were connected, using a barbed socket connector, to 3 mL Luer lock syringes (Terumo) that served as the ink reservoirs. These reservoirs were connected to a back pressure regulation system (MicroFab) using more PTFE tubing. The back pressure was required to prevent the ink from dripping out of the nozzle due to gravity, the regulation system was set to provide a back pressure of -8 mbar [8]. The printer stage and printing heads were all controlled by a custom-made LabView program. This program could control several printing parameters and accept a bitmap to define the geometry of the sample to be printed. The pixel pitch, which is the distance between each pixel can be adjusted in both the X and Y stage movement directions. A Biofluidix software was used to control which printer head was active and to prime both heads such that they both dispensed 50 nL per drop at a frequency of 10 Hz. The samples were printed on a mesoporous substrate called Novele (Novacentrix), this material was used because of its effectiveness in retaining printed geometries using nanothermite inks [13]. Figure 2.2 shows the dual-nozzle printing system in action.

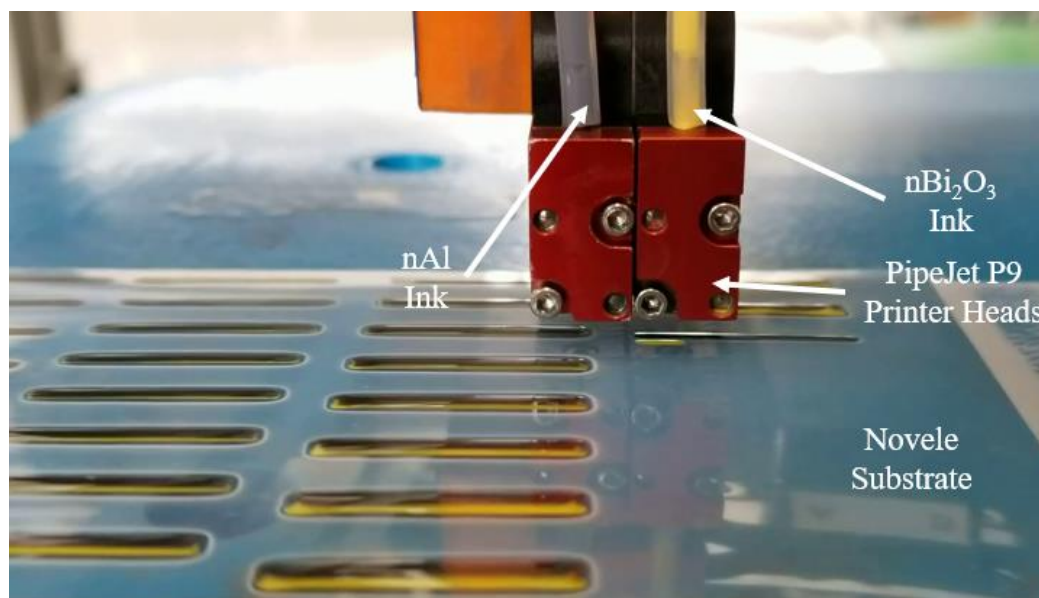


Figure 2.2 Inkjet printing system in dual-nozzle configuration depositing a bilayer sample

2.2.2.1 Determining Printer Settings

To determine the optimal printing parameters to produce high-quality bilayer samples, both inks were analyzed separately before creating the samples used for burning rate measurements. The main parameters to be determined were the pixel pitches, and a number of layers to print for each ink. The bitmap defining the geometry of the samples to be printed was fixed as a 2x40 rectangle. Then each ink was analyzed by printing the same geometry while varying the pixel pitch from 0.4 to 0.7 mm/pixel. A camera fixed above the printer stage, adjacent to the printer heads, was then used to determine the dimensions of the dried samples. A custom-made picture stitching Matlab code was used to extract the dimensions from a composite picture of the dried samples. The averages of the dimensions of 1-layer samples of each ink are compared against each other in Figure 2.3. Three to four samples were analyzed for each pixel pitch setting. The objective of this study was to select the pixel pitch that would result in both constituent inks having the most similar geometries as possible. Thus, from the above plots, pixel pitch settings of 0.5 and 0.7 mm/pix appeared to be the most promising. Note that the large discrepancy in the theoretical width and actual widths of the samples is due to the ink spreading out slightly as it dries. Another quality of the samples that is desired for this study is relatively smooth edges without ridges, such that there is minimal variability along the length of the bilayer samples. Samples printed using each pixel

pitch were analyzed qualitatively using a digital microscope (Hirox). Select images of nAl samples are shown Figure 2.4. As seen in the microscopic images, samples printed using a pixel pitch of 0.7 mm/pixel have significantly rougher edges with several ridges when compared to the sample printed with 0.5 mm/pixel setting. Similar results were seen with the oxidizer ink although not shown here for the sake of brevity. Thus, a pixel pitch of 0.5 mm/pixel setting was used along with just 1-layer of each fuel and oxidizer ink for printing the bilayer samples.

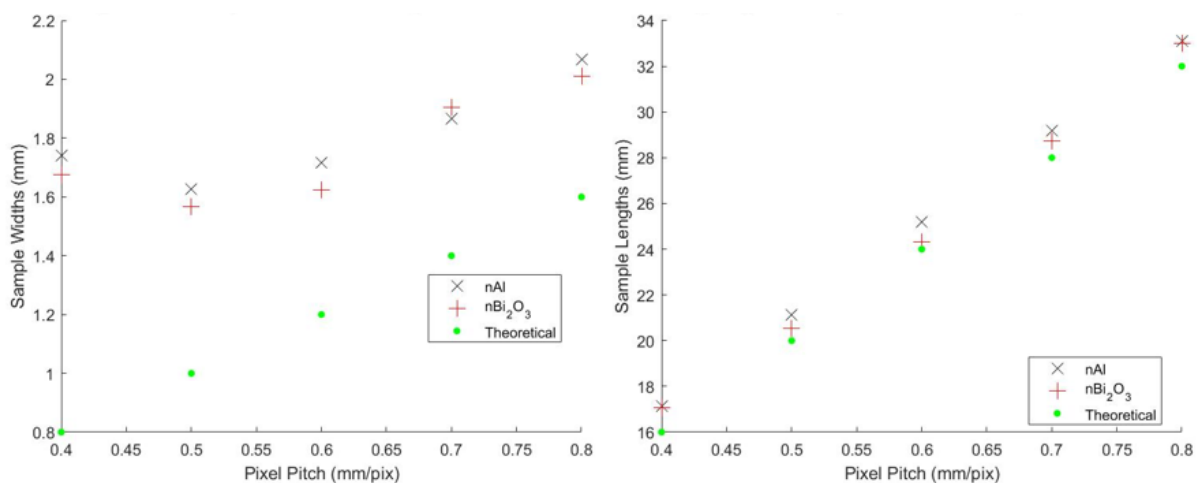


Figure 2.3 Dimensions of dried nAl and nBi₂O₃ samples versus printer pixel pitch

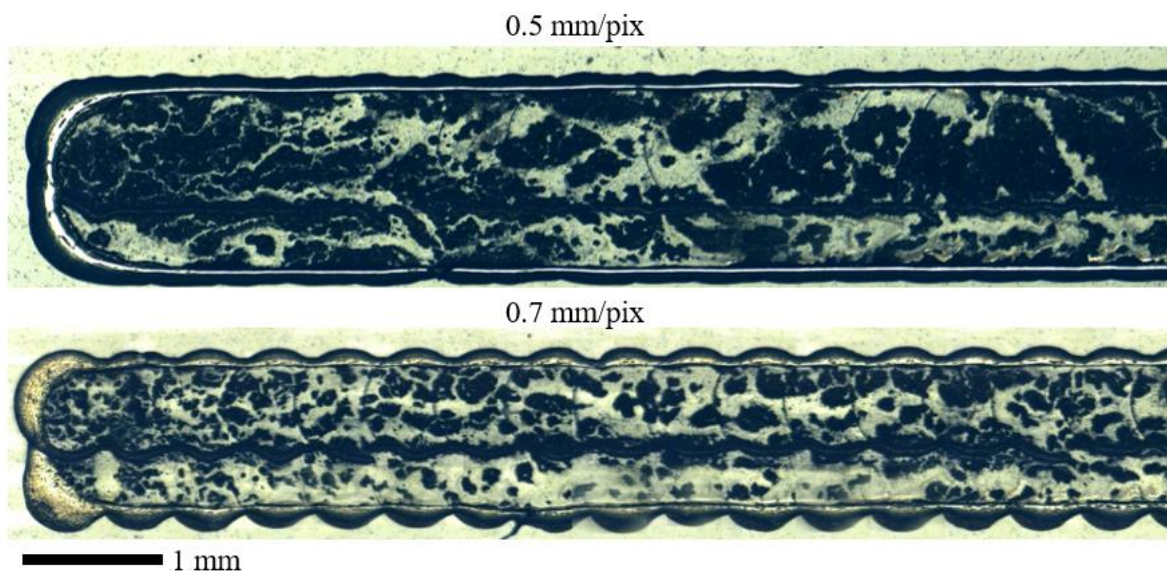


Figure 2.4 Microscopic images of dried nAl samples printed using different pixel pitches

2.2.3 Burning Rate Measurements

The primary measurements made in this study involved acquiring high-speed videos of the bilayer samples burning. Burning rates provide quantitative results to determine how the bilayer thickness affects the combustion performance of this nanothermite system. The samples were ignited using coiled 28 gauge nickel chromium (Nichrome) resistance wire. The Nichrome wire was positioned to be in direct contact with one end of the sample and was then resistively heated using a DC regulated power supply unit (BK Precision 1692). The combustion event was captured using a BW Phantom v7.3 high-speed camera at a frame rate of 40,000 frames per second. The videos were captured at a resolution of 352x64, an exposure time of 23 μ s, and the aperture of the lens was set to f-11. Burning rates were extracted from the videos using a custom Matlab code that accounted for the set frame rate and converted pixels to units of length using a calibration image. This Matlab code allows the user to manually track the flame front. Since the flame front of the burning samples wasn't uniform, the leading edge of it was tracked. The code determines the average burning rate by performing a least-squares linear regression on the position data versus time. The slope of the position of the flame front versus time is taken to be the average burning rate. Figure 2.5 below depicts the set-up used to capture videos of the burning samples.

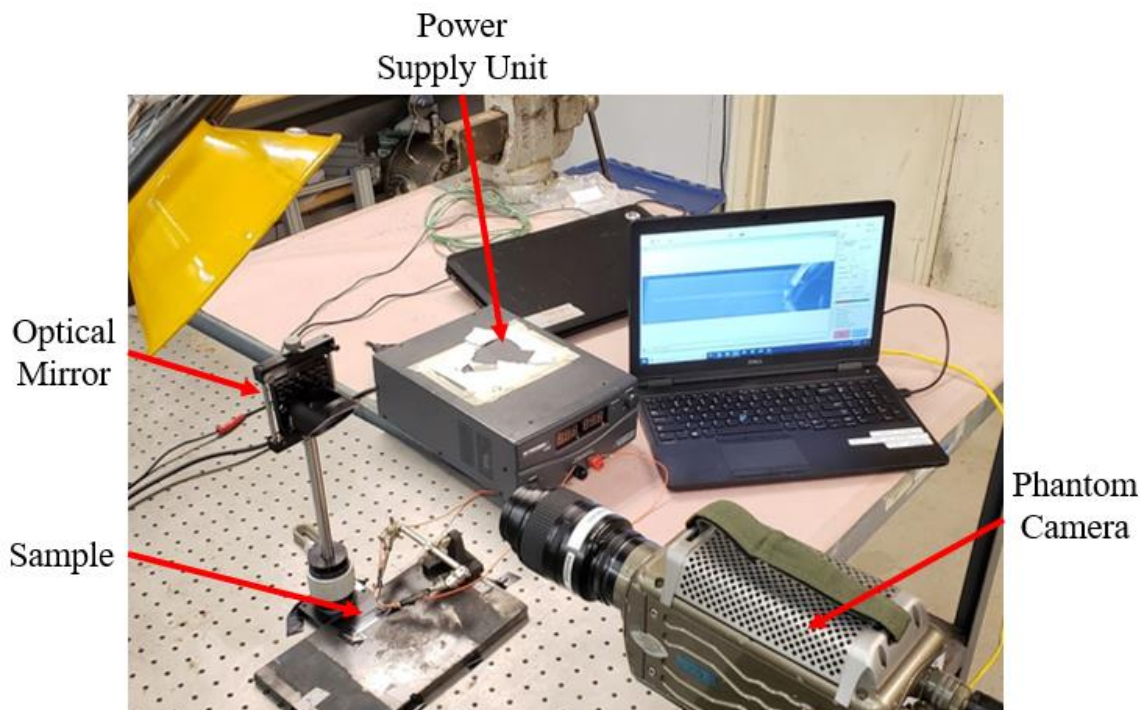


Figure 2.5 Typical experimental set-up used for burning rate measurements

2.3 Results and Discussion

The settings for the samples used in the final analysis are as follows. Samples were created by printing one layer of nAl ink followed by a layer of nBi₂O₃ ink at a prescribed offset distance, i.e. bilayer thickness. Each layer of ink was printed using a bitmap geometry that defined a 1x60 pixel rectangle using a pixel pitch of 0.5 mm/pixel. The offset distance was varied from 0 mm to 1.8 mm in increments of 0.2 mm. This range was chosen because an offset distance of 0 mm corresponds to the layers of fuel and oxidizer ink completely overlapping and 1.8 mm was the maximum offset distance at which the samples would still completely burn. Forty samples were tested in total, using three to four samples at each offset distance. Burning rate videos were captured using the method and settings explained in the previous section. Figure 2.6 shows timestamped screenshots from a sample video.

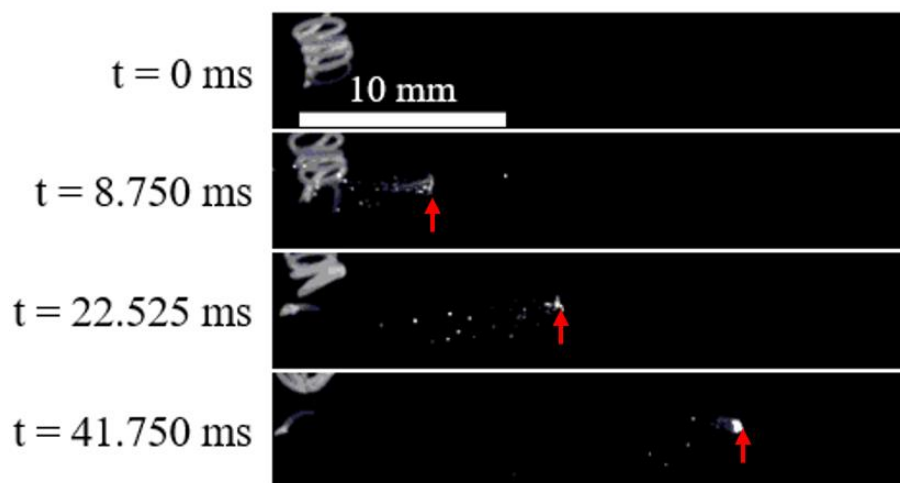


Figure 2.6 Images from a burning rate video of a 1.0 mm offset bilayer sample showing the propagation of the flame front

After all of the samples were burned, the videos were analyzed individually using the aforementioned Matlab code to extract burning rates. The results of the burning rates versus the offset distance between layers of fuel and oxidizer ink layers are summarized in Figure 2.7. The average burning rates are plotted and the error bars represent the standard deviation of each group of samples. In other words, the error bars encompass one standard deviation above and below each plotted average. The results of the burning rate study don't show a significant trend as seen in the figure above. Plotting a trendline to fit the data did not elucidate a clear trend either as the overall trendline has a very slight negative slope. Thus, the trendline was not included here. To confirm

that there was no trend to discern from the data, a statistical analysis method called analysis of variance (ANOVA) was utilized. The ANOVA method provides a statistical test to determine if the population means of multiple groups can be considered equal. A one-factor ANOVA test was used because there is only one independent variable or factor in question here, the bilayer thickness or offset distance. Using a significance level of 0.05, the results of the ANOVA test indicate that the null hypothesis is accepted because the p-value was determined to be 0.0923, which is higher than the significance level. The null hypothesis, in this case, is that the means of each group of samples tested in this study can't be considered statistically different, i.e. there is no statistical difference between the burning rate means.

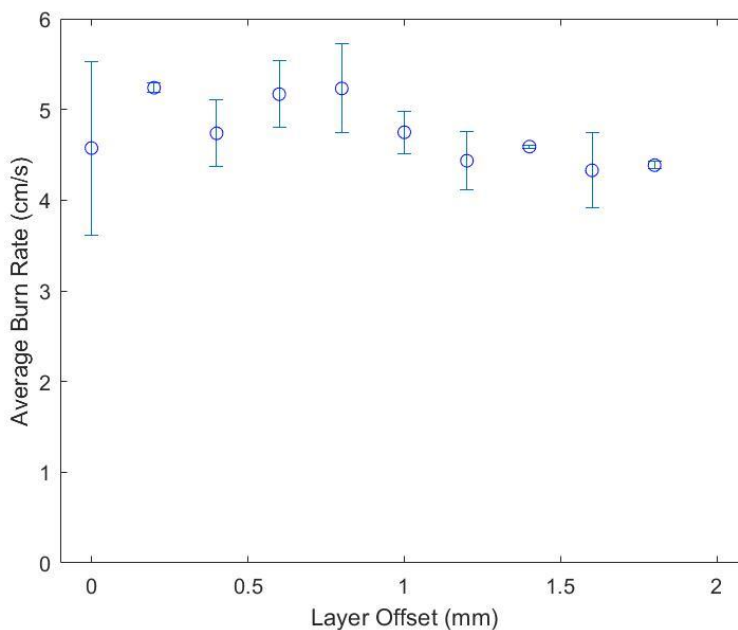


Figure 2.7 Al-Bi₂O₃ nanothermite bilayer sample burning rates versus offset distance

This lack of a trend suggests that the diffusion scale, which is set by the bilayer thickness, does not majorly influence the propagation rate. This result would corroborate the argument by Asay, et al. that convective or non-diffusive processes dominate in nanoscale particle reactive systems [21], [23]. If the diffusion scale was a dominant factor, one would expect to see a clear trend of decreasing burn rate with increasing offset distance. Generally comparing the burning rates of the 0 mm offset distance samples to other similar samples printed using pre-mixed ink, the former (~5

cm/s) is two orders of magnitude slower than the latter (~250 cm/s) [13]. This suggests that even though the separate inks were prepared at the same equivalence ratio, pre-mixed samples will achieve much faster burn rates than the dual ink samples. This discrepancy is most likely explained by a lack of intimate mixing between the aluminum and bismuth oxide (III) in the dual ink setup. Printing one layer of each ingredient directly over the other does not facilitate thorough enough mixing of the nanoparticles in the same manner as acoustic mixing; the solvent likely evaporated before the powders could mix completely in situ [13]. This discrepancy in performance between the dual ink and pre-mixed ink is also in line with the observations made by Murray, et al [8].

3. INKJET PRINTING OF HIGH NITROGEN ENERGETIC MATERIALS

3.1 Introduction

This chapter of the thesis focuses on efforts to synthesize and characterize the performance of high nitrogen inks made using BTATz and DAATO_{3.5}. These materials were chosen due to their favorable insensitive characteristics, as well as their exceptional combustion performance. There are four major parts to the research presented here where the first are thermal stability tests using DSC analysis. Next are burning rate experiments to quantify the performance of the inks. Third, closed pressure cell tests were conducted to quantify the gas production capabilities of the inks. Finally, preliminary thrust force tests were done to characterize the performance of the inks when used in an SPM configuration. However, the first methods detailed here pertain to the formulation of the high nitrogen energetic inks.

3.2 Materials and Methods

3.2.1 Ink Formulation

There are several parameters to consider when formulating an ink for use with inkjet printing to ensure sample reproducibility. Some of the important characteristics for energetic inks include homogeneity (no agglomeration), low viscosity, and high enough solids loading to allow for deposition of useful amounts of EMs. Initial ink formulation efforts began with determining a solvent to use with BTATz. Inks that carry particles are generally classified as a suspension, solution or a supersaturated solution. This first requires using a compatible solvent to create the ink. From a literature review, a few studies that aimed to recrystallize BTATz crystals using polar solvents were identified [24]. Some of these solvents include DMF, dimethylsulfoxide (DMSO), N-Methyl pyrrolidinone (NMP), pyridine, and sulfolane. All of these solvents were acquired to be tested as they are known to dissolve BTATz. Additionally, these solvents are all polar which is beneficial when printing onto a mesoporous substrate called Novele (Novacentrix). This substrate was used because of its effectiveness in retaining printed geometries using nanothermite inks [13]. Initially BTATz was added to samples of the solvents at the proper molar ratio to create a saturated solution. The solutions were mixed using a stir rod and hot plate for 24 hrs and then deposited onto glass slides where they were allowed to dry. The resulting depositions were then analyzed using a

digital microscope to qualitatively compare how different solvents affect the recrystallization of BTATz.

Next a binder was selected to use with the solvent to provide structure to the printed geometries and to adhere HN particles to the substrate. Polyvinylpyrrolidone (PVP, Sigma Aldrich) was selected due to its compatibility, nontoxicity and the fact that it has been successfully used in other ink formulations [8]. Additionally, PVP is known to work as a surfactant, dispersant, and as a shape controlling agent in this type of application [25]. The final ink parameter to be determined was the solids loading and the percent inclusion of the binder. These parameters were determined over several trials using the piezoelectric inkjet printer. Printing tests were conducted until a formulation was reached where the printer nozzle wouldn't clog, and sample reproducibility in terms of mass and geometry was achieved.

All of the inks used in subsequent tests were prepared in centrifuge tubes (VWR) by loading the high nitrogen powders in first and then pipetting in the proper amount of solvent/binder solution into the tubes. Then the ink was mixed using a vortex mixer (Fisher Scientific) and placed in an ultrasonic bath (Branson, Inc.) for 30 minutes prior to printing or depositing.

3.2.2 Inkjet Printing

An inkjet printing system that was developed and used in previous studies was utilized in this study [8], [12], [13]. The printing system utilized a piezoelectric actuated Pipejet P9 (Biofluidix) printing head. The printer head was fixed above a dual-axis linear positioning stage (Aerotech Planar DL 200-XY, 200 mm travel, 0.5 μm accuracy). 500 μm diameter P9 nozzles were attached to one end of approximately 2 cm long pieces of polytetrafluoroethylene (PTFE) tubing with an inner diameter of 1.6 mm. The other ends of the PTFE tubing were connected, using a barbed socket connector, to 3 mL luer lock syringes (Terumo) that served as the ink reservoirs. These reservoirs were connected to a back pressure regulation system (MicroFab) using more PTFE tubing. The back pressure regulation is required to prevent the ink from dripping out of the nozzle due to gravity. The regulation system was set to provide a back pressure of -8 mbar [8]. The printer stage and printing heads were all controlled by a custom-made LabView program. This program could

control several printing parameters and accept a bitmap to define the geometry of the sample to be printed. The pixel pitch, which is the distance between each pixel can be adjusted in both the X and Y stage movement directions. Biofluidix software was used to control which print head was active and to prime both heads such that they both dispensed 50 nL per drop at a frequency of 10 Hz. All of the samples were printed on Novele substrates. Figure 3.1 shows the printing system in action.

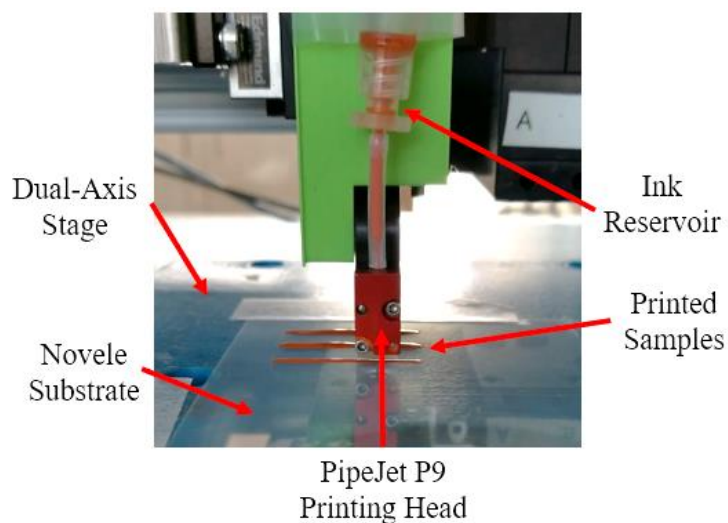


Figure 3.1 Inkjet printing system depositing BTATz-DMF-PVP ink

3.2.3 Thermal Stability Analysis

To determine the thermal stability characteristics of the high nitrogen energetic inks, thermal gravimetric analysis (TGA) and differential scanning calorimetry (DSC) were performed. Dried BTATz and DAATO_{3.5} ink samples were analyzed and compared against pure BTATz and DAATO_{3.5} powder samples using DSC/TGA (SDT Q600, TA Instruments). All of the sample masses were kept low around ~1.5 mg to avoid damaging the equipment. Tests were conducted at two heating rates of 10 and 20 °C/min across a temperature range of 25 to 450 °C. A steady flow rate of 40 mL/min of ultra-pure argon (99.999 vol.%) was used. The goal of these experiments was to determine if the thermal sensitivity of the HN materials was modified by the ink formulation (binder and surfactant addition).

3.2.4 Burning Rate Measurements

The samples were ignited using coiled 28 gauge nickel chromium (Nichrome) resistance wire. The Nichrome wire was positioned to be in direct contact with one end of the sample and was then resistively heated using a DC regulated power supply unit (BK Precision 1692). The combustion event was captured using a BW Phantom v7.3 high-speed camera. For BTATz burning rate measurements, the camera settings used were 400x104 pixels, a frame rate of 400 frames per second, an exposure time of 2498 μs , and a lens aperture setting of f-2.8. For DAATO_{3.5} samples, the same resolution and aperture settings were used, but the frame rate was set to 1000 frames per second and the exposure time was 998 μs . The purpose of this study was to characterize the combustion performance of samples printed using HN and to compare BTATz and DAATO_{3.5} against each other. Additionally, the effect of confinement on the burning rate of printed BTATz was investigated. Kapton tape (DuPont), which is a type of polyimide film, was applied on top of the sample to act as the confiner. Burning rates were extracted from the videos using a custom Matlab code that accounted for the set frame rate and converted pixels to units of length using a calibration image. This Matlab code allows the user to manually track the flame front. Since the flame front of the burning samples wasn't uniform, the leading edge of it was tracked. The code determines the average burning rate by performing a least-squares linear regression on the position data versus time. The slope of the position of the flame front versus time is taken to be the average burning rate. Figure 3.2 depicts the set-up used to capture videos of the burning samples.

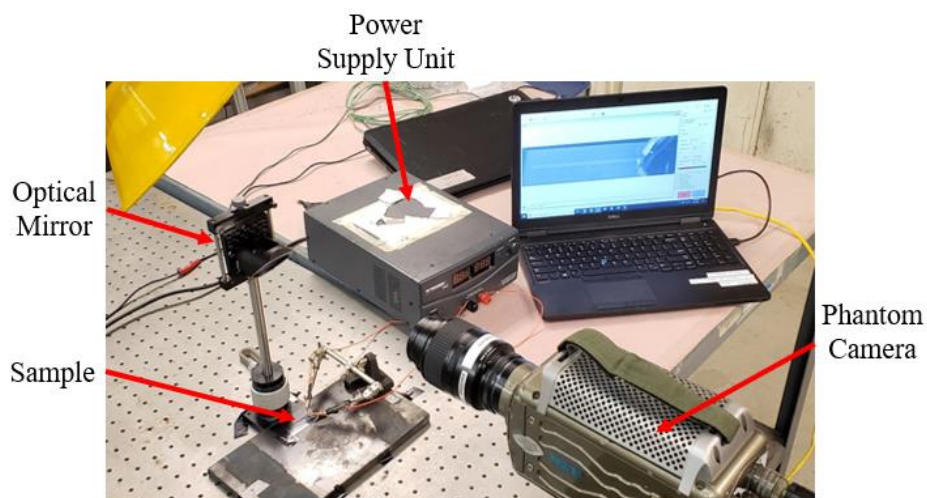


Figure 3.2 Experimental set-up used for burning rate measurements

3.2.5 Closed Pressure Bomb Experiments

In order to characterize the gas producing performance of both HN inks, a closed stainless steel Parr cell with a volume of 130 mL was utilized. The HN inks were deposited using a micropipette onto sticker samples that were made using vinyl tape and Novele substrate. Several of these samples were prepared with both types of ink, with varying volumes of ink deposited. Once the ink was dried, a Nichrome wire coil was placed on top of the ink with the leads protruding out of the sticker. The vinyl sticker was then folded to confine the dried ink and to ensure contact between the Nichrome wire and the ink. The range of volumes went from 25 to 125 μL in increments of 25 μL . All the ink used for these experiments were prepared at 20% solids loading with 5% PVP in DI water. This type of sample is shown in Figure 3.3.



Figure 3.3 Sticker samples drying with varying amounts of deposited BTATz ink

These sticker samples were ignited via Nichrome wire inside of the Parr cell to contain the combustion gases. The Parr cell was outfitted with two types of pressure transducers. One dynamic piezoelectric sensor (PCB 113B27) with a range of 0-100 psig, and one static sensor (WIKA Type A-10) with a range of 0-25 psig. These sensors were calibrated using a calibration system (Omega DPI 610). The static sensor was powered using a DC power supply (BK Precision 1692). The dynamic sensor was connected to a signal conditioner (PCB 482A22). Data from the pressure

transducers was collected using a 100 MHz oscilloscope (Rigol DS1104Z). A pre-trigger was used on the oscilloscope to capture some data before the trigger level was reached. The Parr cell is also fitted with a high pressure power line passthrough (Conax C3963-2) to connect the power supply to the Nichrome ignition wire. Flat alligator clips were soldered onto the ends of the copper power lines that were internal to the Parr cell. These clips were used to secure the power connection to the Nichrome wire that was in contact with the samples. The other end of the passthrough power lines were attached via wire nuts to a 5 A, 0-130 V variable AC (Variac) transformer (Anesty, TDGC2-0.5KM). This Variac provided the power to resistively heat the Nichrome wire inside the Parr cell to ignite the sample. The Parr cell experimental setup can be seen in Figure 3.4. The purpose of these experiments was to study the pressure rise that can be achieved by combusting these high nitrogen inks and the rate of pressurization. Data from the dynamic pressure sensor was used to quantify the pressurization rate in the range of data between 10 and 90 percent of the peak pressure. The static sensor was used to provide peak pressure data but was not used to analyze the transient pressurization event. A Matlab code was developed to smooth the data collected from the sensors using a moving mean calculation and extract the peak pressures and pressurization rates. In addition to these experiments, there were efforts at using simplified thermochemistry models to compare the experimental data against theoretical values. The thermochemistry calculations and data analysis methods are discussed in more detail in the results and discussion section.

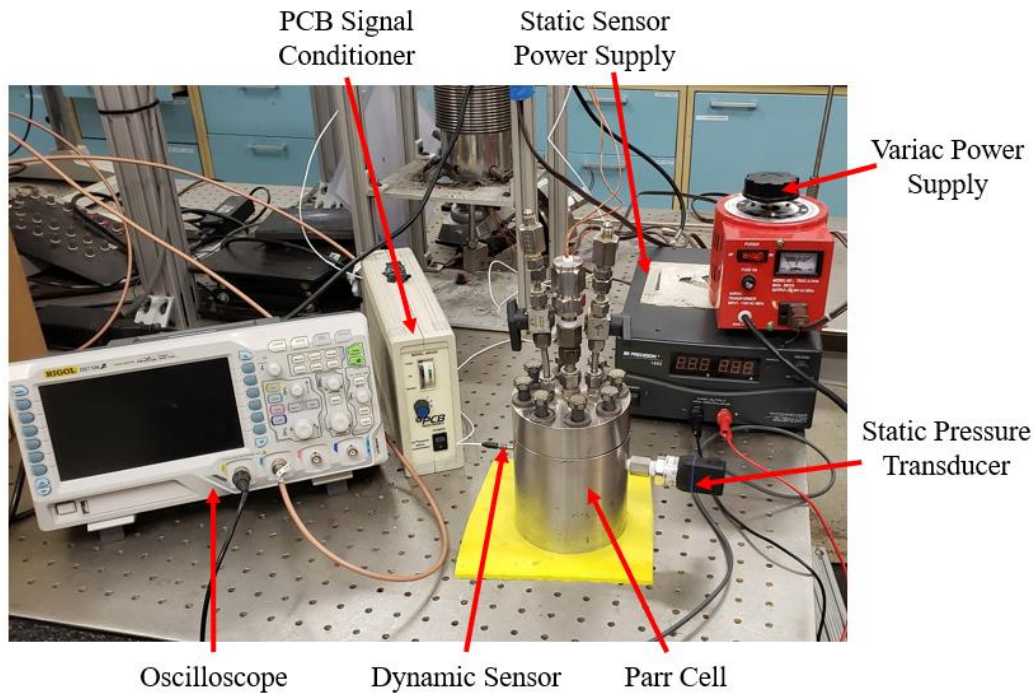


Figure 3.4 Parr cell experimental setup

3.2.6 Microthruster Experiments

Parts for the microthruster assembly were 3D printed (Ultimaker 3) using polycarbonate filament with 80% infill. Polycarbonate was chosen over acrylonitrile butadiene (ABS) due to its higher melting temperature and higher tensile strength [26]. A simple two-part microthruster design was drafted using CAD software. The assembly is comprised of a chamber and a press-fit cap that provides confinement to allow the chamber pressure to rise while the propellant combusts. The cap was designed to be ejected after ignition to allow for the pressurized combustion gasses to leave the chamber and provide thrust without fracturing the walls. This press-fit cap also has a small hole that allows for a Nichrome coil to be threaded through the top of the microthruster. The chamber and cap dimensions (in millimeters) are shown in Figure 3.5. This geometry was selected to accommodate at most 200 μL of wet ink.

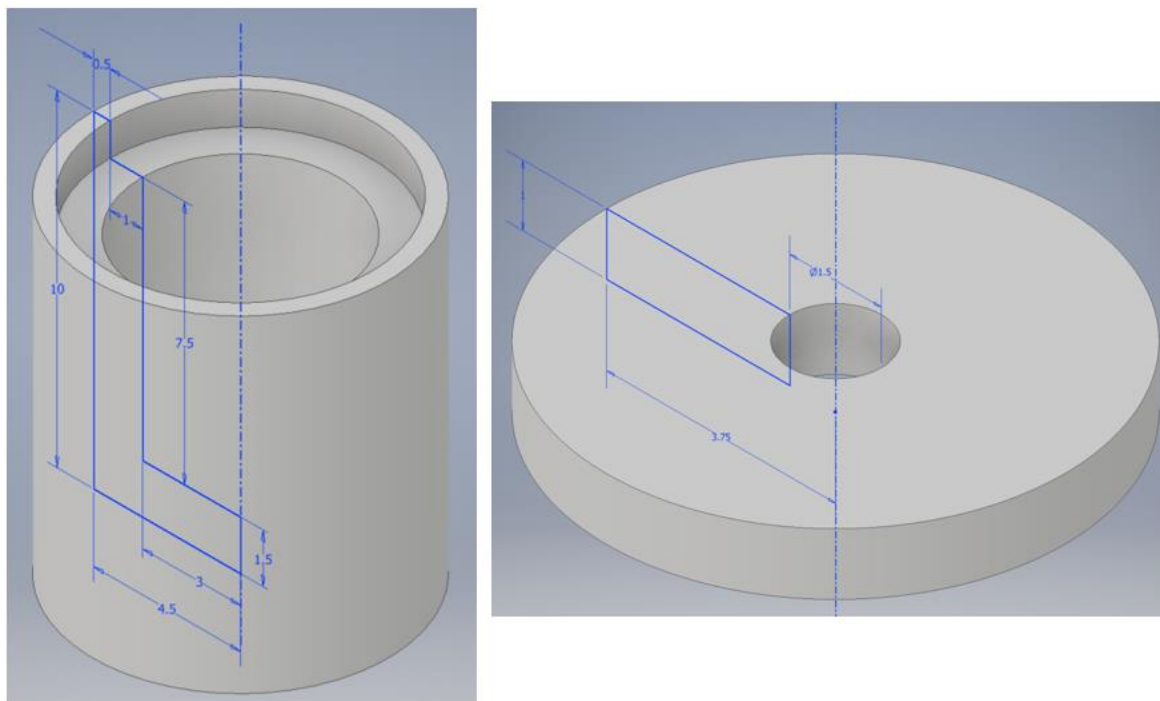


Figure 3.5 Dimensioned CAD renderings of microthruster components in millimeters

Once the parts were 3D printed, varying volumes of the high nitrogen inks were loaded into the chambers using a pipette and were left to dry. Once the ink dried, a Nichrome wire was coiled, and the leads were threaded through the hole in the cap. Next, the cap was pressed into the chamber lip such that the Nichrome coil was in contact with the top surface of the propellant. A top ignition scheme like this was chosen because it has been shown to be more efficient [27]. Finally, a dab of superglue was placed around the Nichrome leads to seal the hole. Samples were prepared at two loading levels of 100 and 200 μL for both types of ink. The same ink formulations that were used for the Parr cell experiments were also used for the microthruster experiments.

After preparing the samples, experiments were conducted using a 0-200 N piezoelectric force transducer (Kistler 9215) to attain thrust traces. A custom-made test stand was utilized to reduce the vibrational noise to the transducer. The force transducer was plugged into a dual mode amplifier (Kistler Type 5010) to convert the charge output to voltage. This amplifier was set to the long time constant option and had a sensitivity and scale of 81.3 pC/N and 5 N/V respectively. The amplifier was connected to an oscilloscope which collected the force data (Rigol DS1104Z) at a sampling rate of 250 MSa/s. The microthruster samples were secured to the thrust stand using

a dab of lubrication grease (Kistler Type 1063). A set of power lines with flathead alligator clips were connected to the Nichrome leads sticking out of the caps of the samples. The leads were suspended over the sample using a lab jack and soldering helper hands to ensure no external force was applied to the samples during tests. These lines were connected to a DC power supply (BK Precision 1692) which provided the current to resistively heat the Nichrome wire and ignite the microthrusters. The experimental setup is depicted and labeled in Figure 3.6.

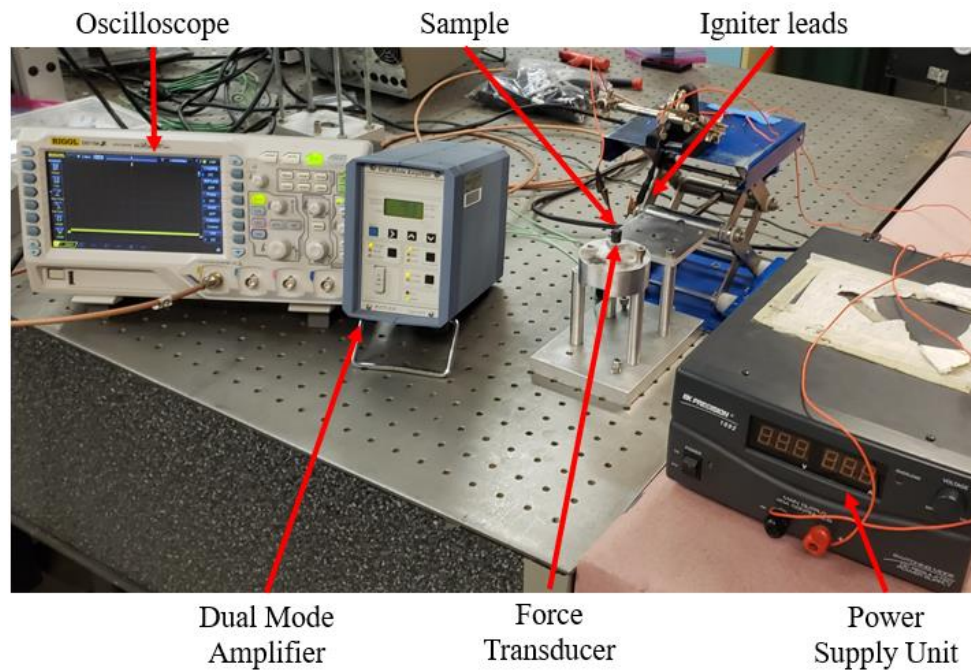


Figure 3.6 Experimental setup used to acquire thrust force traces of microthruster samples

Separate microthruster samples were prepared for obtaining high-speed schlieren videos. The ignition tests were recorded using a Phantom v5.1 color camera (Vision Research) with a Nikon AF Micro Nikkor 105 mm f/2.8 D lens. The schlieren imaging system (Edmund Optics 71-013) used included two spherical aluminized mirrors with diameters and focal lengths of 15.24 cm and 152.4 cm respectively. A green LED was used as the light source and a razor blade was used as a vertical knife edge. Videos were collected at 4,040 frames per second, an exposure time of 2 μ s and a resolution of 512x552.

The main objective of this study was to determine peak thrust, total impulse, and specific impulse values achieved by microthrusters utilizing high nitrogen inks as propellant. However, in addition to thrust force experiments, a microthruster array containing three chambers in a triangular formation was prototyped and tested. The array was designed to use the same caps as the single chambers. Figure 3.7 shows a CAD rendering of the array and the printed part filled with wet BTATz ink. The array samples were not tested for thrust performance, however they were tested to demonstrate the ability to 3D print arrays of microthrusters with a high packing density. Each chamber was individually ignited and recorded with the goal of showing that unintentional ignition of adjacent chambers is not a concern.

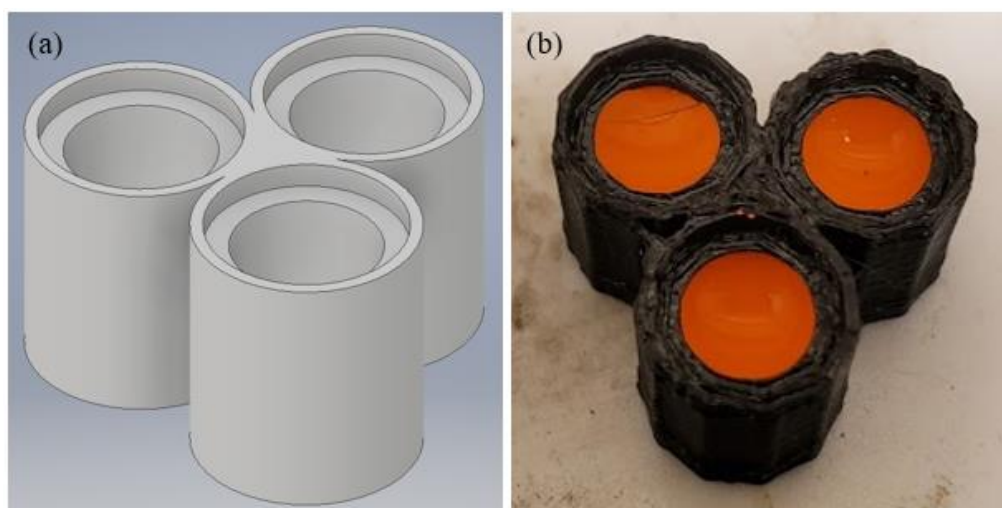


Figure 3.7 (a) CAD rendering of microthruster array and (b) 3D printed array loaded with wet BTATz ink

3.3 Results and Discussion

3.3.1 Ink Formulation Results

As discussed in the materials and methods section, the ink formulation study began with selecting an appropriate solvent. Figure 3.8 shows an image taken of BTATz recrystallized from DMF using a digital microscope (Hirox) with side lighting. Qualitative analysis using the digital microscope revealed that using DMF produced relatively small crystals uniformly distributed throughout the sample. This can be compared to the crystals created when using DMSO as the solvent. The top

lit microscopic images in Figure 3.8 and Figure 3.9 show the resulting BTATz crystal structure when using DMF and DMSO respectively as the solvent. The crystals seen in Figure 3.9 are different than those created using DMF in that they are larger and have a rod-like shape. This crystal shape was also observed by Saikia, et al. in their study on the dissolution and crystallization of BTATz [24]. Solvent tests using sulfolane, pyridine and NMP all produced similar results; however, they were ruled out as potential solvents due to their toxicity and relatively high boiling points. Lower boiling points (higher volatility) are desired for the solvent used in the ink because that translates to shorter drying times.



Figure 3.8 Recrystallized BTATz using DMF as the solvent



Figure 3.9 Recrystallized BTATz using DMSO as the solvent

One test was performed using n-hexane to create a suspension with BTATz particles, the suspension was deposited on a glass slide and analyzed using the microscope as well. Figure 3.10 shows a microscopic image taken of the sample using top lighting. The n-hexane suspension was not effective at producing a homogenous dried sample because the BTATz particles never dissolve. This also caused the BTATz particles to settle out of the n-hexane very quickly which is not favorable for the printing application. Although n-hexane has a very low boiling point, this non-polar solvent was ruled out due to its inability to dissolve BTATz.



Figure 3.10 Dried BTATz deposited as a suspension with n-hexane

DMF was eventually selected as the solvent to move forward with since it produced uniform results in the recrystallization test and has been used in previous ink formulations with nanothermite. Although not one of the initial solvents tested, distilled (DI) water was also used as a solvent to create inks using both HN materials. DI water proved to be effective in dissolving BTATz, DAATO_{3.5} and binders. DI water also has positive characteristics such as having a relatively low boiling point and being nontoxic. The ink formulation using DI water became necessary during the microthruster experiments due to incompatibility issues with DMF and 3D printed polycarbonate parts.

Once the DMF/PVP and DI water/PVP formulations were shown to work successfully with BTATz, they were also used and tested with DAATO_{3.5}. The final ink formulations used with the printing system included 25% and 15% solids loading by mass for BTATz and DAATO_{3.5} respectively. These ink formulations also included binder at a ratio such that 5% of the solids mass was PVP. In total, four types of inks were used in this study; BTATz-DMF-PVP, BTATz-H₂O-PVP, DAATO_{3.5}-DMF-PVP, and DAATO_{3.5}-H₂O-PVP. An Excel spreadsheet was created to take inputs of desired volume of ink, solids loading by mass, and PVP inclusion percent to calculate the necessary masses and volumes of all of the ink constituents for each of the four ink types.

Microscopic images were also taken of dried printed samples to qualitatively assess the print quality. Figure 3.11 shows an image taken at 350x magnification with top lighting of a BTATz sample printed with an ink formulation using DMF and PVP at a solids loading of 25% by mass. As seen in the image, the particle sizes appear to be fine and uniform. Figure 3.12 shows an image of printed DAATO_{3.5} with an ink formulation using DMF and PVP at a solids loading of 15% by mass. Again, the particle sizes shown appear to be fine and uniform.



Figure 3.11 Microscopic image of an inkjet printed BTATz sample on Novele substrate



Figure 3.12 Microscopic image of an inkjet printed DAATO_{3.5} sample on Novele substrate

3.3.2 DSC/TGA Results

The BTATz samples used in this analysis were formulated with DMF at 20% solids loading by mass with 5% PVP. The DAATO_{3.5} samples used the same formulation except at 15% solids loading. However, the dried mass of the ink samples were all approximately 1.5 mg. In total, eight samples were analyzed. Pure BTATz powder and BTATz ink were both analyzed at two heating rates of 10 and 20 °C/min. This same test matrix was executed for DAATO_{3.5} powder and ink as well. Note that the TGA results for the pure HN materials at the 20 °C/min heating rate resulted in a spike in the weight percent. This was likely due to the heating rate being too high and causing the material to ignite rather than decompose. It is also suspected that the combustion gases imparted a thrust force on the internal scale causing the results to be unreliable. Thus, TGA data collected from those cases are not presented here. Additionally, only absolute heat flow values are reported. Figure 3.13 compares the heat flow behavior of pure BTATz powder against that of the BTATz ink. The results show that the higher heating rate resulted in a higher onset temperature compared to the lower heating rate. This can be explained by a thermal lag effect. It is likely that the lower heating rate allowed for the dried BTATz ink to absorb enough heat to cause the surface

temperature to surpass its initiation temperature before the higher heating rate case. Since the temperature is being ramped up twice as rapidly in the higher heating rate case, the surface temperature of the BTATz likely has a delay in equilibrating to the temperature inside the furnace.

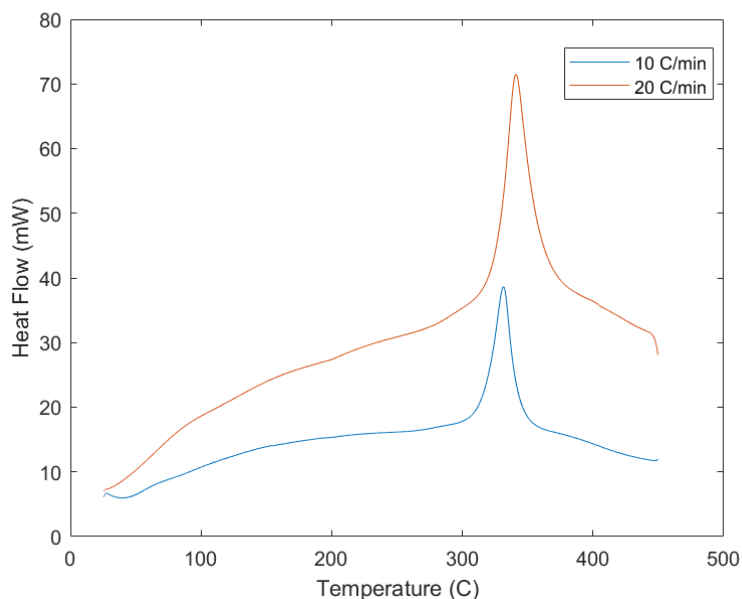


Figure 3.13 DSC results comparing two BTATz ink samples at different heating rates

Figure 3.14 shows the disparity in thermal stability between BTATz and DAATO_{3.5} inks. The DAATO_{3.5} ink is clearly more sensitive to thermal stimuli and has an onset temperature nearly 100 °C lower than that of BTATz. However, the mass loss of BTATz appears to be slightly more rapid. Additionally, the heat release of the DAATO_{3.5} sample is more gradual which corroborates the difference in the slopes of the mass loss curves. This result is important as a safety consideration for using these types of inks in an inkjet printing system that utilizes a heated printer head.

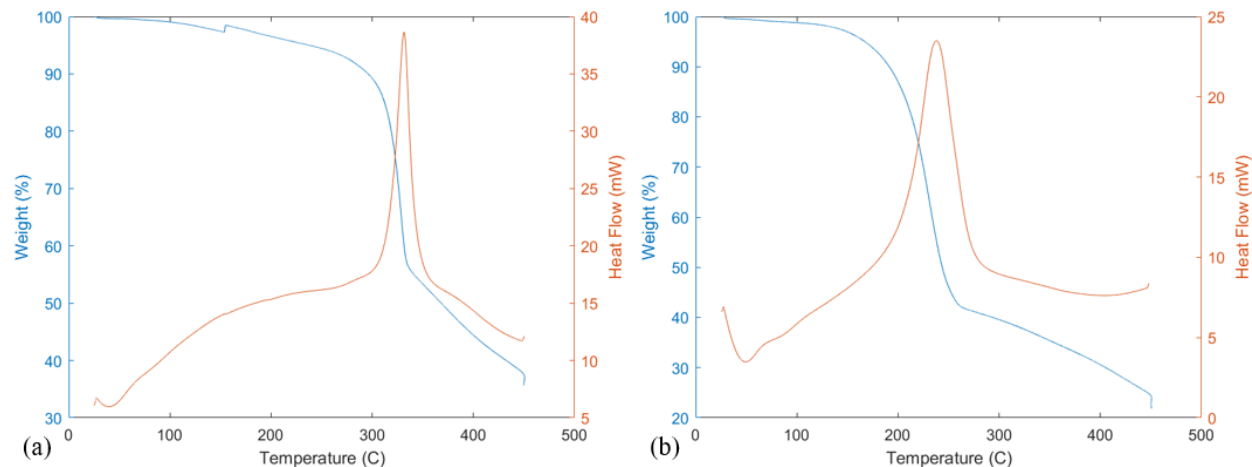


Figure 3.14 DSC/TGA data for (a) BTATz and (b) DAATO_{3.5} inks at a heating rate of 10 °C/min

Table 3.1 summarizes the thermal stability data obtained for tests done at a heating rate of 10 °C/min. The lower heating rate is used for discussion because it represents a worse case than the 20 °C/min due to the thermal lag phenomena mentioned previously. The DSC data shows that the BTATz ink is slightly more thermally stable than pure BTATz. The peak exotherm occurs at ~331 °C for the ink while the peak for the pure substance occurs at ~322 °C. The onset temperature for the ink was determined to be ~296 °C which can be compared to the onset of pure BTATz which has been reported to be around 264 °C. This improvement in thermal stability can most likely be attributed to the inclusion of an inert binder in the ink. The DAATO_{3.5} ink formulation was also analyzed using DSC/TGA and compared against the as received powder. Interestingly, unlike as seen with BTATz, the DSC onset temperature for DAATO_{3.5} ink samples appears to be slightly lower than that of the base material. Ali, et al. reported that adding small percentages of polyvinyl alcohol and triethylene glycol reduced the onset temperature of DAATO_{3.5} but decreased its spark sensitivity [20]. Overall the heat release of the DAATO_{3.5} ink sample appears to be more gradual when compared to the pure sample. Thus, it can be argued that the DAATO_{3.5} ink is also slightly more thermally stable than the pure substance. Again, this is most likely due to the inclusion of the inert PVP binder that acts like a heat sink. However, the thermal stability improvement is more significant for the BTATz ink.

Table 3.1 Summary of thermal stability results at a heating rate of 10 °C/min

Material	Onset Temp. (°C)	Peak Heat Flow Temp. (°C)
Pure BTATz	282.3	321.6
Pure DAATO _{3.5}	178.5	246.4
BTATz Ink	295.8	331.4
DAATO _{3.5} Ink	176.4	238.1

3.3.3 Burning Rate Results

The main factors studied in the burning rate experiments were the number of printed layers and the ink formulation. Additionally, a confinement study was conducted on BTATz ink samples to determine how the burning rate is affected. The first study aimed to quantify how the binder inclusion level affects the burning rate when keeping the overall solids loading constant at 25% by mass. Four BTATz ink formulations were used in this test. The PVP inclusion percent was varied at the following levels; 0, 2.5, 5 and 10 percent. Additionally, the number of printed layers from was varied 1 to 7 layers with an increment of 2 layers for each batch of ink. Three samples were printed at each setting meaning a total of 48 samples were tested. The points plotted in Figure 3.15 are the average burning rates and the error bars represent one standard deviation above and below the mean. As expected, the case with 0 wt% PVP inclusion had the highest burn rates regardless of the number of layers. This is most likely because there is theoretically no relatively inert material in those samples once the solvent dries. An unexpected result was that the burning rate consistently decreases with an increasing number of layers in almost all of the cases except the case with no binder. This could be explained by incomplete combustion where the upper layers of material are thrown off due to the combustion gases and thus don't fully contribute to the propagation speed. Overall, all of the burning rates recorded are within a relatively small range 0.26-0.36 cm/s. The print quality is also an important factor for some of the potential applications of this technology. From qualitative observations during these experiments, higher binder inclusions resulted in better printed geometries and reduced the samples' susceptibility to flaking. Based on these observations and the fact that there was no clear trend to discern about the effect of binder inclusion on the burning rate, a 5% binder inclusion by mass was utilized for subsequent Parr cell and microthruster experiments. This binder inclusion percentage was also employed for the DAATO_{3.5} ink formulation used to print burning rate samples.

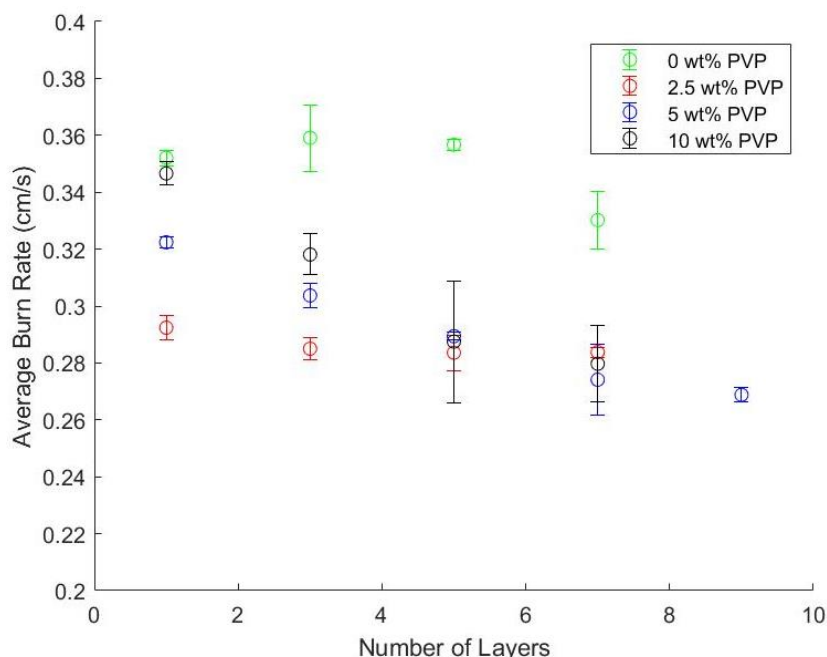


Figure 3.15 Burning rate of BTATz ink at varying binder inclusion levels and layers

The next study investigated the effect of confinement, using Kapton tape, on the burning rate of BTATz samples. These samples were printed using the same formulation described above with 2.5% binder inclusion by mass. The number of layers was varied again and a total of 24 samples were analyzed. In Figure 3.16 just as before, the plotted points represent average burning rates while the error bars represent one standard deviation above and below the average. Note that the unconfined burning rates plotted are multiplied by 10 to allow for easier comparison. The results of this study show that confinement can increase the burning rate by over an order of magnitude. However, the variability significantly increases when confining samples. This variability may be explained by cracks that formed in the samples while applying the Kapton tape. Cracks and other deformations in the confined sample likely contributed to the increased burning rate and large variability. This shift in speed could be an indication of a change in the propagation mechanism from diffusive burning to convective burning. Interestingly, in the confined case, increasing number of layers seems to increase the burning rate whereas the opposite effect was seen in the unconfined samples. This may confirm the theory that in unconfined printed samples, a good amount of material may be blown away before combusting. In the confined configuration, this material gets caught by the tape and eventually combusts. If more complete combustion is occurring in the confined configuration, this may partly explain the increase in burning rates.

Figure 3.17 shows time stamped images taken from high-speed videos of unconfined and confined samples burning with arrows indicating the location of the flame front.

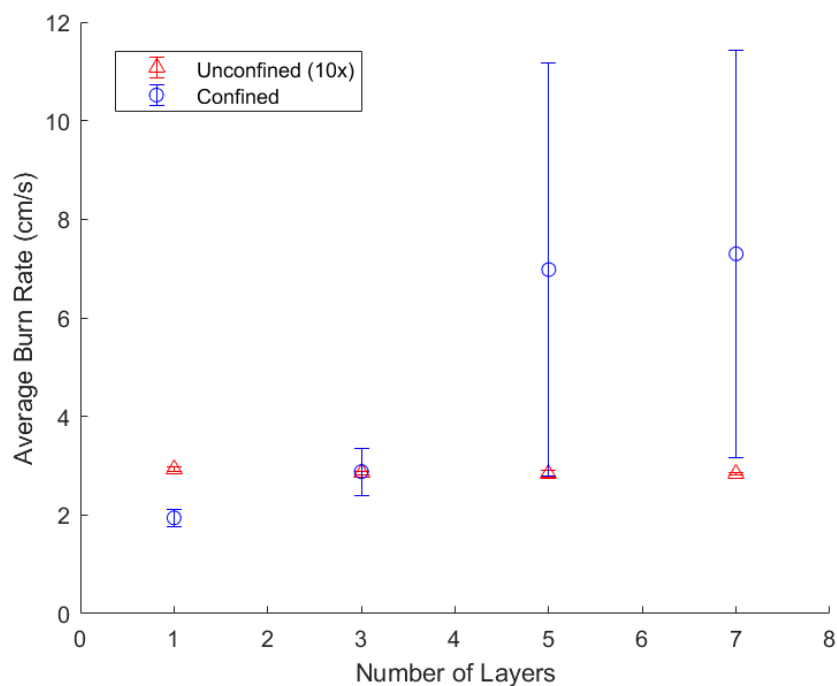


Figure 3.16 Confined versus unconfined printed BTATz burning rates

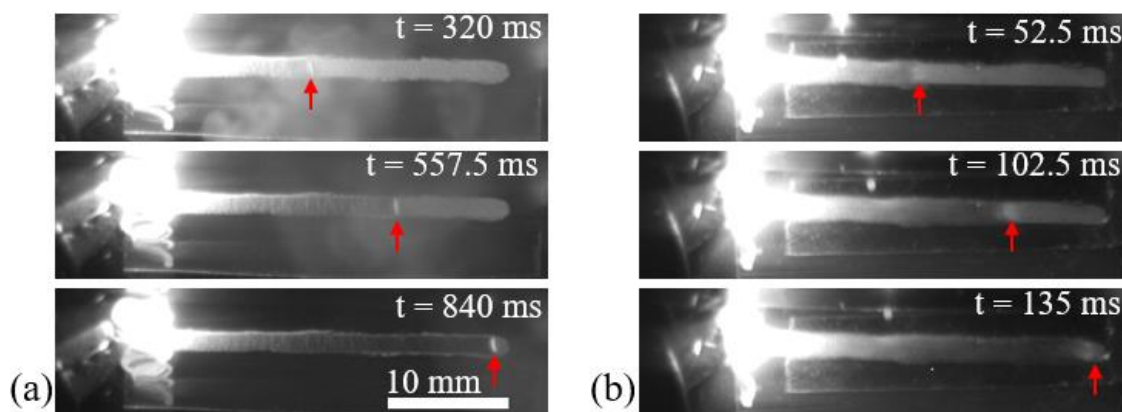


Figure 3.17 High-speed images of burning (a) unconfined and (b) unconfined BTATz samples

Samples were printed using DAATO_{3.5} ink as well; however, maintaining a high solids loading in the ink proved to be more difficult for this material, which is known to have a porous structure [20]. After several printing tests, the ink formulation was optimized to achieve sample repeatability

and avoid clogging in the PipeJet nozzle while printing. The ink formulation that was used to print burning rate samples used DI water as the solvent with 15% solids loading and 5% PVP by mass. The samples were printed using the same printer settings and geometry as used for the BTATz samples. The number of printed layers was varied from 1 to 7 with an increment of 2 layers. The camera frame rate and exposure time settings were adjusted to account for the faster burning DAATO_{3.5} samples as mentioned in Section 3.2.4. In total, 18 DAATO_{3.5} samples were analyzed, the burning rate results are plotted in Figure 3.18. Again, the plotted points represent the averages while the error bars represent the standard deviation. The burning rates are overlaid with results from a similar BTATz ink formulation for comparison. The BTATz burning rates correspond to the 25% solids loading and 5% PVP by mass ink formulation. The DAATO_{3.5} samples had burning rates nearly double that of the corresponding BTATz samples. This result was expected as it has been reported in literature that DAATO_{3.5} may be one of the fastest burning organic solids known [18], [20]. From these burning rate results, it is clear that the number of printed layers does not seem to significantly affect the propagation speed. Interestingly, the DAATO_{3.5} samples showed a slight increase in burning rate when three layers are printed versus one layer. However, above three layers the speed gradually decreases which is the behavior also observed for the BTATz samples.

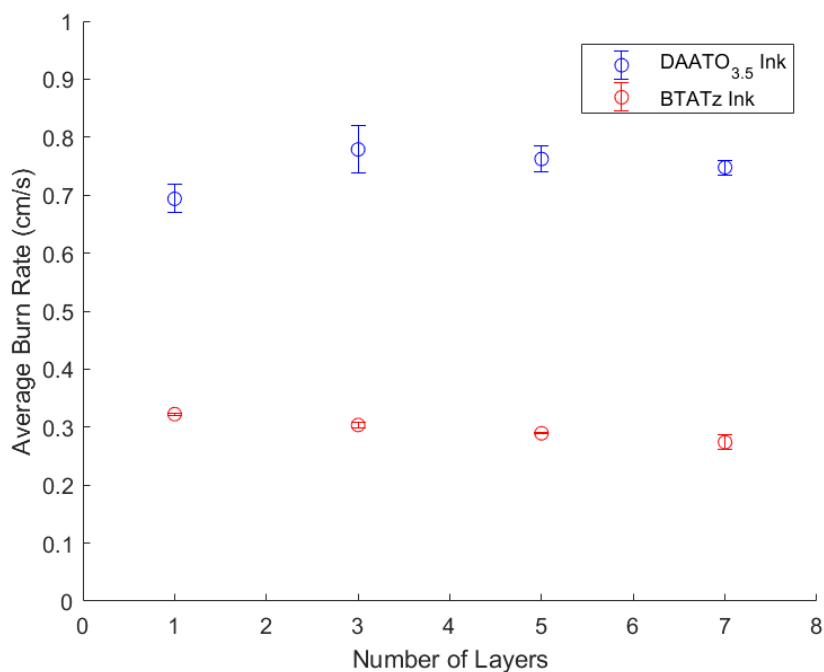


Figure 3.18 Comparison of DAATO_{3.5} and BTATz ink burning rates

3.3.4 Parr Cell Results

3.3.4.1 Experimental Results

Several samples of both inks were analyzed using the Parr cell test setup described in the Materials and Methods section. The inks used in these experiments were prepared using the same solids loading (20%) and binder inclusion (5%) to allow for direct comparisons of the different HN materials. Samples were prepared by using a pipette to deposit the inks by hand onto the Novele/vinyl stickers. The volume deposited was varied from 25 to 125 μL in increments of 25 μL . The memory depth of the oscilloscope was set to save 700,000 data points for all of the tests. However, the time range over which the data was collected varied. For BTATz samples, pressure data was recorded over a time range of 140 ms. Since the DAATO_{3.5} samples had much slower pressurization rates, data was collected over a time range of 1.4 seconds. The dynamic pressure sensor's data was used to determine the pressure rate since it had a faster response time than the static sensor. The peak dynamic pressure was determined, and a linear fit was applied to match the slope of the pressure rise from 10 to 90% of the peak value. This method can be visualized in Figure 3.19 which displays example traces for both types of ink. The data shown in Figure 3.19 is for one sample of each ink, the volume deposited was 75 μL which translates to a dried HN mass of 16.815 mg for both types of ink. These pressure traces show the gap in both peak pressures and pressurization rates between the two inks. The BTATz samples significantly outperformed the DAATO_{3.5} samples in both measures. This result was expected since BTATz is known to produce a more significant amount of gas per unit mass, reported theoretical volume of gaseous products has been reported as 1,237 L/kg [14],[24]. However that large of a disparity between the two materials was not expected.

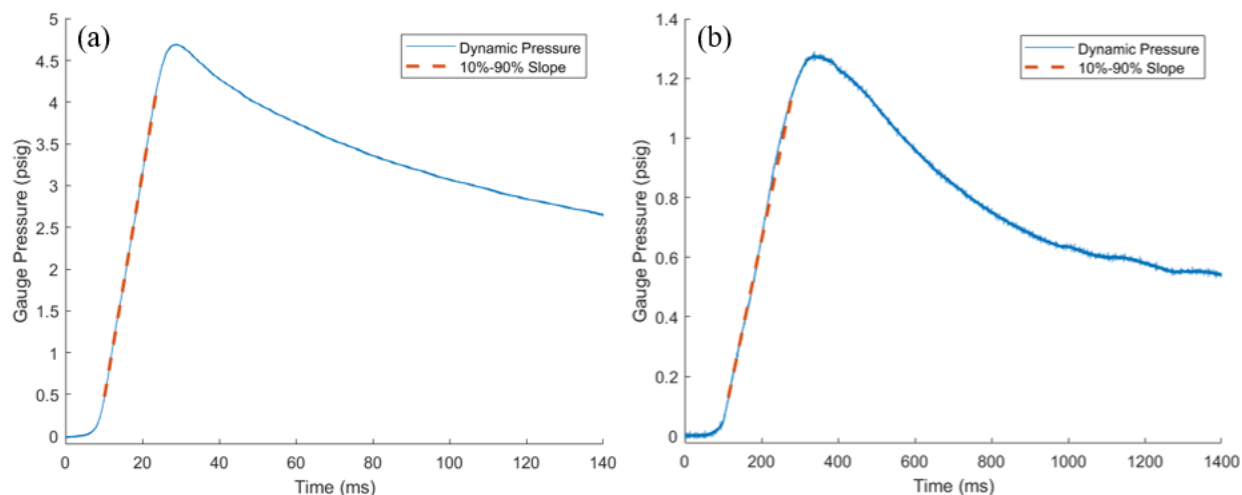


Figure 3.19 Comparison of dynamic pressure traces for (a) BTATz ink and (b) DAATO_{3.5} ink

In total, 22 BTATz samples and 17 DAATO_{3.5} samples were analyzed using the Parr cell set-up. The peak static pressures achieved by the samples are summarized in Figure 3.20. The average peak pressures are plotted against the dried mass of EM in the samples, and the error bars represent the population standard deviation. Figure 3.20 clearly shows the disparity in peak pressures generated by the two inks. Both data sets show upwards linear trends in peak pressure as the sample mass is increased. Figure 3.21 plots the pressurization rates seen for both ink types. The plots were not overlaid due to the BTATz samples having pressurization rates nearly two orders of magnitude higher than those of the DAATO_{3.5} samples. Again, the averages are plotted with standard deviation error bars. The overall trend seen for both data sets is an increase in pressurization rate with increasing sample mass which was expected. However, the variability in the data was quite high. The variability may be explained by variability in confinement between the sticker samples, the addition of inert material from the vinyl residue, and incomplete combustion. The main observation made here is that even though DAATO_{3.5} ink proved to have faster a burning rate, its pressurization rate is slower than that of BTATz ink that produces more gas.

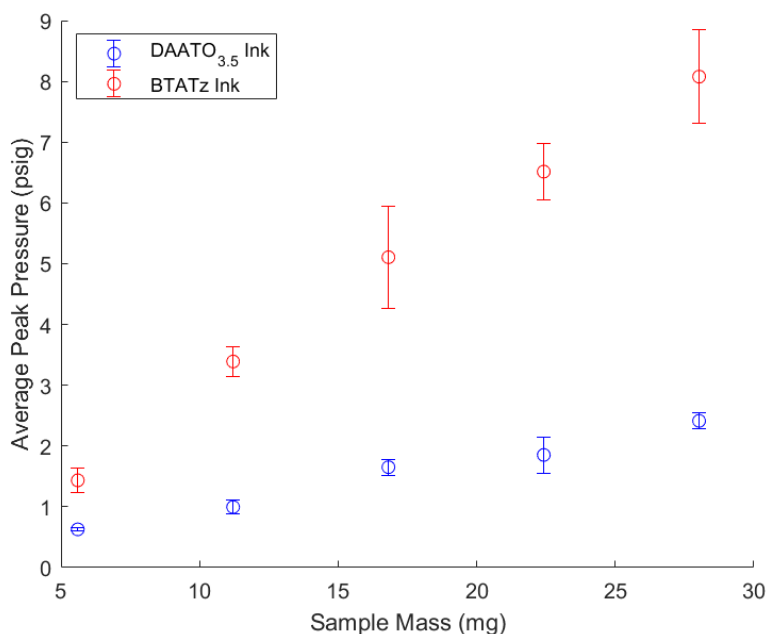


Figure 3.20 Comparison of peak static pressures generated by BTATz and DAATO_{3.5} samples

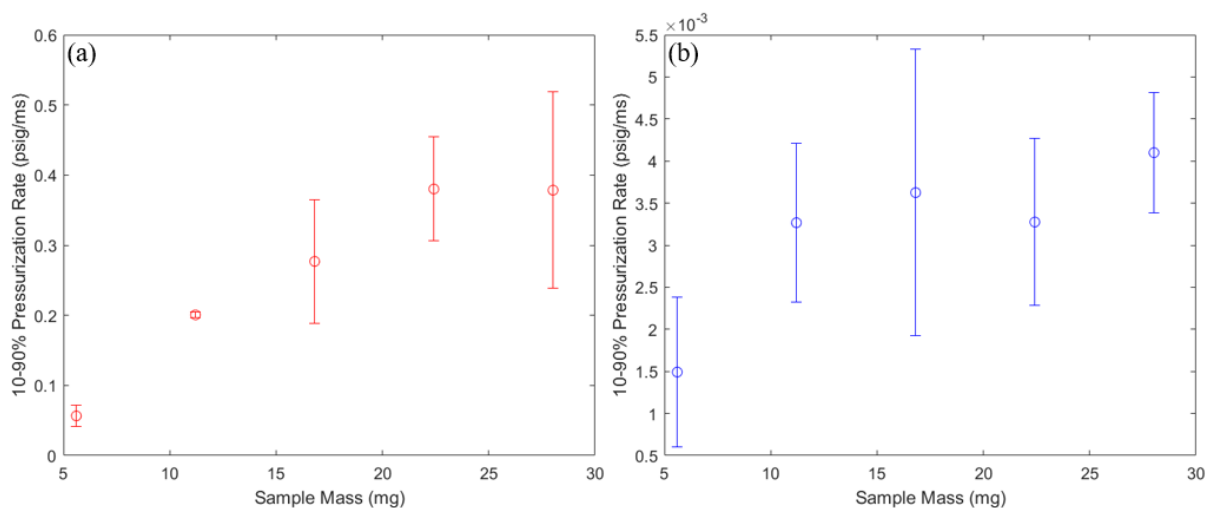


Figure 3.21 Comparison of pressurization rates for (a) BTATz ink and (b) DAATO_{3.5} ink

3.3.4.2 Thermochemistry Calculations

Two thermochemistry models were utilized to compare the experimental pressure rise values against theoretical calculations. The first theoretical model used a thermochemical equilibrium software called CHEETAH 7.0 that was developed by Lawrence Livermore National Laboratory [28]. A constant volume explosion problem template along with the JCZ3 product library was

utilized. Five cases were executed for each type of ink to reflect the five sample masses tested for both materials. The reactants were entered in the form of a volume percentage which was calculated using the known volume of the Parr cell and the known densities of the EMs and atmospheric air. The CHEETAH software tends to overestimate pressures because of its ideal assumptions including no heat losses and complete combustion. In order to account for some of these losses that were observed during experiments, the same set of simulations were ran using argon instead of air since reaction with the air is probably minimal. Note that the inclusion of PVP in the samples was not included since that material was not available in the reactants library. Only the mass of the dried energetic material and surrounding ambient air (or argon) was included in the calculation. The results of these two studies are shown in Figure 3.22. These theoretical values are essentially an order of magnitude larger than the experimental results. There are several potential explanations for this discrepancy; however, most stem from the idealized assumptions that are likely not applicable to this particular test setup. One of these assumptions is that the high nitrogen material is perfectly mixed throughout the closed volume which the enclosed gas. However, this is obviously not accurate since the energetic material is enclosed inside a sticker within the Parr cell. It is also likely that the combustion gases lost a significant amount of heat to the stainless steel walls of the Parr cell causing the temperature and subsequently the pressure to drop. Additionally, visual inspection of the combustion chamber revealed several solid particles and some unburnt material. This is likely another major source of the discrepancy between theoretical and experimental values. The CHEETAH simulation assumes that nearly all the combustion products are gaseous; however, this is not the case in reality.

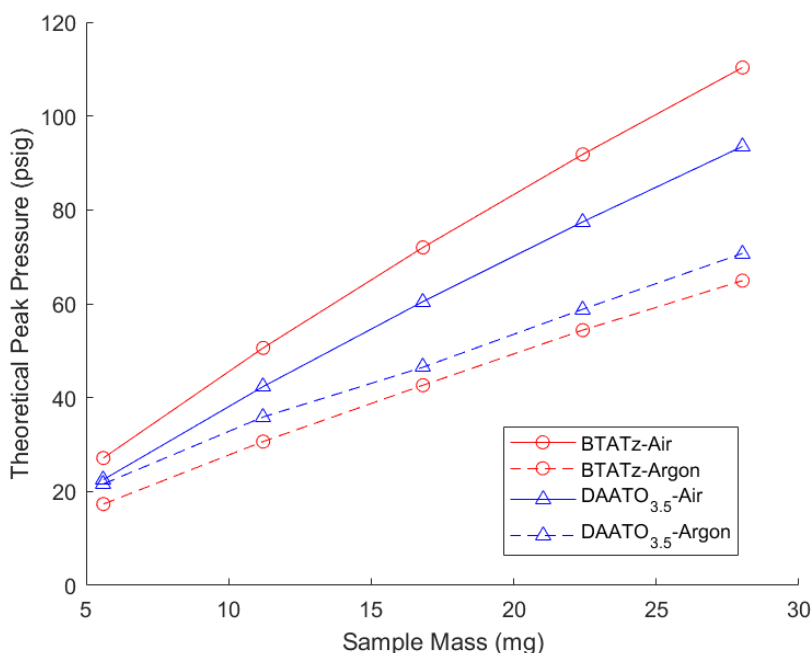


Figure 3.22 Predicted peak pressures determined using CHEETAH simulations

In order to more closely model the experimental results, a simplified ideal combustion model using frozen chemistry was developed. The main assumptions of this model are that the combustion is considered ideal and completed without the interaction of the surrounding air in the Parr Cell. Additionally, the product gases are assumed to instantaneously cool to room temperature. Any products that are generally condensed at room temperature were ignored in the final pressure calculation. The ideal gas law was used to calculate the theoretical pressure in the Parr cell. Note that for this simplified model, the PVP content was assumed to be negligible and ignored. The chemical equations assumed for the BTATz reaction is:



Note that the four moles of carbon are ignored in the pressure calculation since it is a solid. The chemical equation assumed for DAATO_{3.5} is:



A Matlab code was developed to compute the volume of gaseous products for the given sample mass and the assumed reaction equation. The results of this simulation for both materials are overlaid in Figure 3.23. The major conclusions from the modeling efforts and experimental data is that both results agree that BTATz outperforms DAATO_{3.5} in terms of peak pressure. Of the models presented, one significantly overpredicts the experimental data; however, the other slightly

underpredicts. Since the CHEETAH model makes several idealized assumptions, it serves as the upper bracket. The second simplified model has assumptions that are likely closer to the actual experimental conditions. The simplified model's predictions serve as a lower bracket for potential peak pressure values. Thus, the experimental data lies between the trendlines of the two theoretical models presented here.

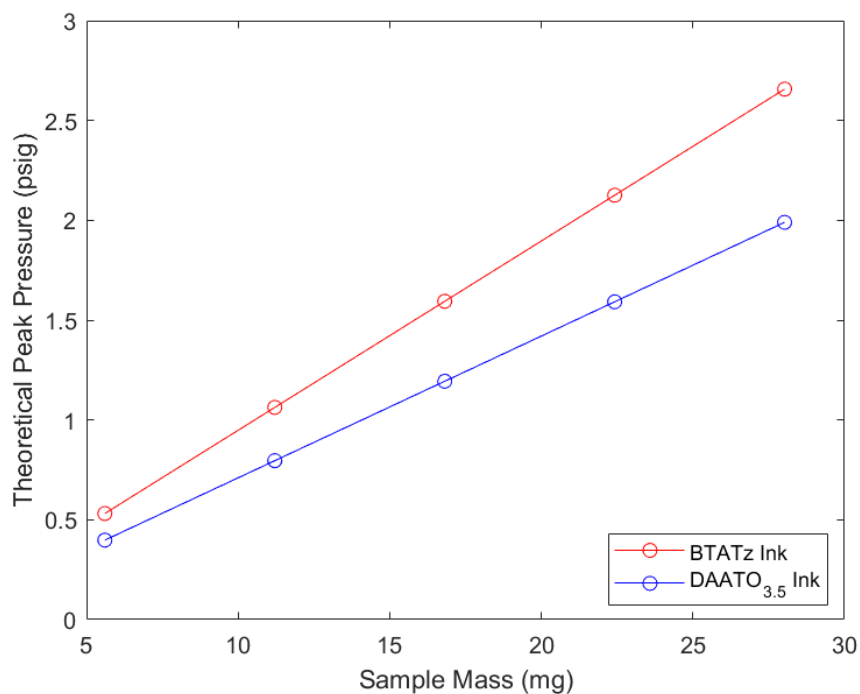


Figure 3.23 Theoretical pressures calculated using simplified thermochemistry model

3.3.5 Microthruster Results

As mentioned in the materials and methods section, four types of microthruster configurations were analyzed for their performance. The four configurations varied the volume of ink deposited in the chambers and the type of ink used. Samples were prepared with 100 and 200 μL of both types of ink. In total, 16 microthrusters were tested. The thrust force data was analyzed using a custom Matlab code that plotted the data and determined the peak thrust, total impulse, and specific impulse. Total impulse is of interest because it defines the change in momentum that the microthruster can provide. The equation used to calculate total impulse is,

$$I = \int F dt \quad (3.3)$$

where I represents the total impulse, F represents the thrust force, and t represents time. Total impulse was calculated using a built-in Matlab trapezoidal integration function. The starting and end points for integration were determined by establishing a baseline voltage output from the transducer with no input force. The point at which the voltage rose above and below this baseline voltage was used as the integration range. Specific impulse is another important parameter which essentially is an efficiency measure that represents the ratio of the thrust produced to the weight of the propellant used. The equation used to calculate specific impulse is,

$$I_{sp} = \frac{I}{m_p \cdot g_0} \quad (3.4)$$

where I_{sp} represents specific impulse, m_p represents the mass of propellant used, and g_0 represents the gravitational acceleration constant. The mass of propellant was assumed to be the dry mass of high nitrogen material in the chamber for these calculations. Figure 3.24 shows example thrust traces that were obtained during experiments. Note that a moving mean filter was utilized for clarity in the plots below. Two thrust traces are shown, one for a sample loaded with 200 μL of BTATz ink and another for a sample loaded with the same amount of DAATO_{3.5} ink. Note that the negative thrust values and oscillatory behavior seen after the peak force are likely due to a ringing effect that all load cells are subject to.

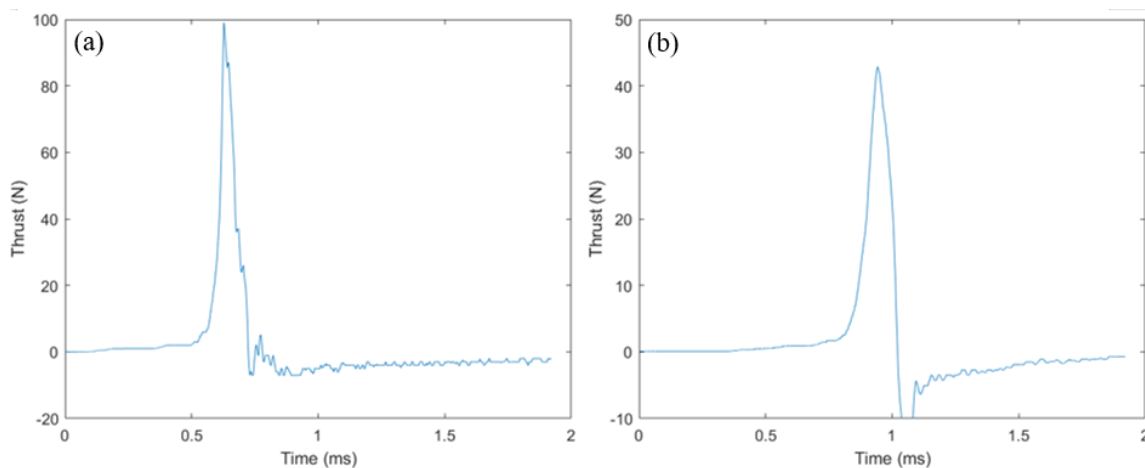


Figure 3.24 Thrust traces for samples filled with 200 μL of (a) BTATz and (b) DAATO_{3.5} ink

High-speed videos of the microthrusters in operation were also collected. Figure 3.25 shows timestamped images of a sample filled with 200 μL of BTATz ink igniting. Figure 3.26 shows

another series of high-speed images taken of a microthruster loaded with 200 μL of DAATO_{3.5} ink. Note that both sets of high-speed images have the same time increment between frames for easier comparison. In all of the microthruster tests, the chamber cap was successfully ejected allowing the combustion gasses to escape and produce thrust. A nozzle was not employed in this design since previous studies have shown that adding a nozzle to microthruster configurations may actually have an adverse effect on performance for fast burning propellants [29]. Additionally, using a press-fit cap ensures that the chamber does not over pressurize and cause the chamber to explode. This is desirable when using microthruster arrays to avoid unintentional ignition of other microthruster units and damage to the microsatellite.

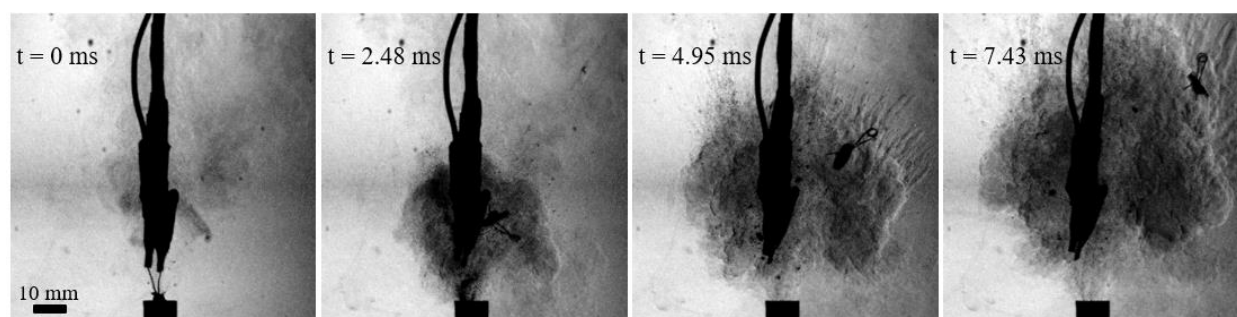


Figure 3.25 High-speed images showing ignition of a microthruster loaded with BTATz ink

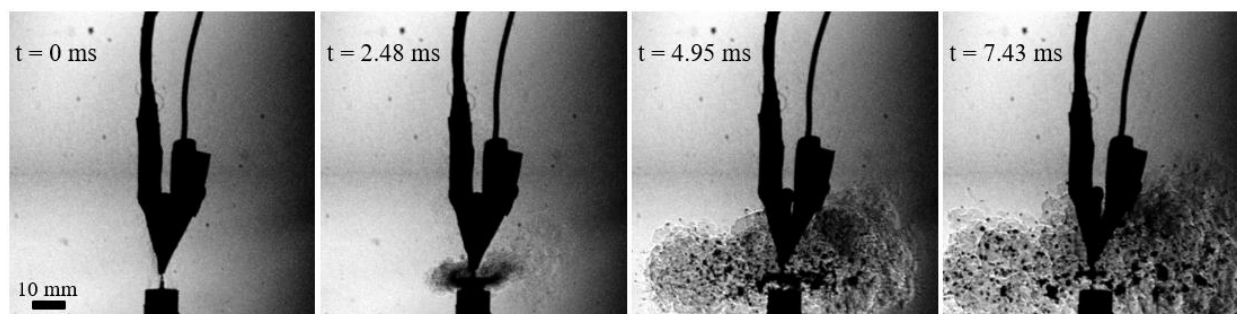


Figure 3.26 High-speed images showing ignition of a microthruster loaded with DAATO_{3.5} ink

The results of the thrust force analysis are shown in Table 3.2 which summarizes the average peak thrust, total impulse, and specific impulse achieved by each microthruster configuration tested. The population standard deviations are also included in the table to show variance. The data shows that generally with increasing propellant loads, the peak thrust and total impulse slightly increase. Interestingly, this upwards trend is not true for specific impulse. For both types of propellant, there

was a significant decrease in specific impulse as the propellant mass was increased. There are several potential reasons for this including incomplete combustion and excessive two-phase flow losses which are common issues in microthrusters [4]. This theory is confirmed by the high-speed videos where several condensed phase particles can be seen exiting the chamber. Frictional and thermal losses to the chamber walls are also common in micropropulsion [29]. Additionally, the data shows that the peak thrust in all of the cases was highly variable. However, the total impulse and specific impulse were less variable. This implies that although the instantaneous thrust produced by these microthrusters was variable, the average force produced during the ignition period was generally more repeatable. Overall, the BTATz samples appear to outperform the DAATO_{3.5} fueled microthrusters in all three of the performance metrics. However, the BTATz samples showed significantly more variability in peak thrust. The BTATz loaded samples were most likely superior due to the fact that this material produces a larger volume of combustion gases compared to DAATO_{3.5}. This has been reported in literature and was confirmed in the Parr cell experiments presented in this work [18].

Table 3.2 Summary of microthruster performance results

Ink Type	Ink Volume (μL)	m_p (mg)	F_{\max} (N)	I (mN·s)	I_{sp} (s)
BTATz	50	11.89	28.59 ± 9.46	2.55 ± 0.45	21.85 ± 3.79
DAATO _{3.5}	50	11.89	10.10 ± 2.03	2.2 ± 0.29	18.89 ± 2.53
BTATz	100	23.75	62.23 ± 14.44	6.03 ± 1.22	25.87 ± 5.26
DAATO _{3.5}	100	23.75	74.64 ± 8.60	4.89 ± 0.90	20.96 ± 3.87
BTATz	200	47.5	69.17 ± 22.85	7.7 ± 1.28	16.60 ± 2.72
DAATO _{3.5}	200	47.5	77.50 ± 18.53	7.57 ± 2.08	14.60 ± 3.87

Microthruster tests using Al-Bi₂O₃ nanothermite and an AP composite propellant were conducted to compare the performance of the HN propellants. Nanothermite ink was prepared at an equivalence ratio of 2 using previously published methods [13]. The composite propellant was prepared at a solids loading of 86% by mass with 80% and 20% coarse and fine AP respectively. The binder used in the composite propellant was hydroxyl-terminated polybutadiene (HTPB). One set of microthruster samples was prepared using 23.75 mg of nanothermite and another set was prepared using the same mass of AP composite propellant. The nanothermite microthruster tests resulted in thrust forces larger than the range of the transducer. The nanothermite fueled microthrusters reacted violently in the confined configuration causing some of the polycarbonate chambers to fracture. None of the AP composite fueled microthrusters were able to eject the

chamber caps and thus, no thrust traces were obtained. The result of these propellant comparison tests show that both HN materials outperform the AP composite but likely produce less thrust than nanothermite. However, the HN inks appear to be more suitable for the confined microthruster configuration than nanothermite. This is because the HN inks produce thrust forces in the desired range for micropropulsion applications and do not destroy the chambers.

A major disadvantage of SPMs is that they are not reusable and inherently “one-shot”. However, this drawback can be mitigated by employing arrays of microthrusters [30]. Due to the thrust performance and relatively low mass of the microthrusters developed in this study, it would be feasible to mount an array arranged in a high packing density configuration onto a Class 1 microspacecraft. With the same AM systems used in this study, scaling these microthrusters to be applicable to smaller or larger spacecraft is possible. Figure 3.27 shows high-speed images taken of the microthruster array in operation. Three arrays were tested in total, all of the chambers were filled with 150 μL of BTATz ink. Force data was not collected due to the geometry of the array which produces off center thrust forces relative to the force transducer resulting in inaccurate readings. Each of the three thrusters in the array were sequentially ignited and recorded. The purpose of this test was simply to demonstrate that when one chamber is ignited, adjacent chambers are not damaged or ignited. The chamber on the left is fired and does not breach the chamber walls or cause the adjacent thruster in the center of the images to ignite. All three of the array tests were successful in that only the chamber being addressed ignited all nine times. The results of these tests show that 3D printed microthrusters using proper filament and infill can be reliably ignited and used in an array configuration. All of the microthrusters tested in this study were ignited using less than 3 V which is well within the desired ignition voltage for application to microsatellites [31]. The primary requirements for SPMs are minimal costs to the mass, power, and volume budgets. Additionally, SPMs should have repeatable and tunable impulse bits. The propellant requirements include high energy density, ability to propagate in small chambers, and fast burning rates. Also, the propellant must be insensitive to thermal, impact, and electrostatic stimuli as well as be vacuum stable. Both BTATz and DAATO_{3.5} have proven to meet the propellant requirements. Thus, the microthruster prototypes developed in this study meet the major criteria for application in spacecraft micropropulsion.

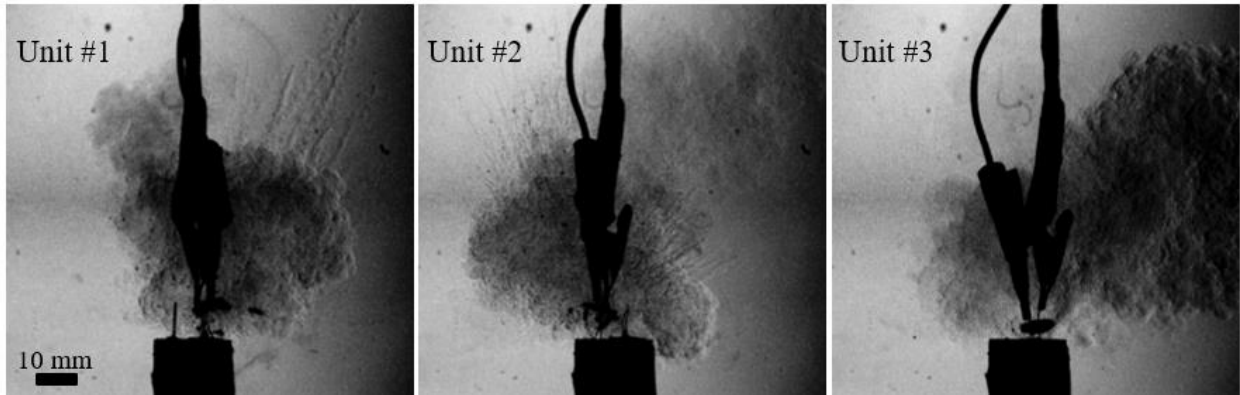


Figure 3.27 High-speed schlieren images of a microthruster array ignition test

4. CONCLUSION

With the continued miniaturization of engineering devices and components, the need for micro-scale power sources is ever more pressing. The integration of EMs with MEMS devices is a promising solution, but the current roadblocks include appropriate manufacturing methods and proper material selection. Recent improvements in piezoelectric inkjet printing technology have enabled selective and precise deposition of energetic inks and may be a solution to the scalable manufacturing of these integrated devices. Using energetic inks with this type of printing system opens countless potential applications, such as micropropulsion and microactuation systems. The work presented in this thesis focuses on two types of energetic inks: nanothermite, and high nitrogen inks.

Nanothermites are a type of MIC that is comprised of a metallic fuel and metal oxide oxidizer. Dual-nozzle inkjet printing allows for combinatorial printing of reactive materials. This type of printing was used to study the fundamental combustion mechanisms seen in Al-Bi₂O₃ nanothermite by utilizing separate fuel and oxidizer inks. Inks were formulated to have an equivalence ratio of 2 and printing parameters were optimized to produce printed lines with smooth edges and similar dimensions for both inks. To study the processes that control the burning rate of nanothermite, bilayer samples were printed with varying bilayer thicknesses between lines of fuel and oxidizer inks. The burning rates of these samples were determined using a high-speed camera to track the propagation of the flame front. The results showed that there was no apparent relationship between the bilayer thickness of samples and their burning rates. Statistical analysis of the data confirmed that there were no significant differences between the average burning rates of each sample group. Thus, it is argued that convective processes dominate the propagation velocity in nanothermite systems rather than the diffusion scale.

The second type of ink studied utilized high nitrogen EMs. BTATz and DAATO_{3.5} are some of the most promising high nitrogen materials from the CHN-tetrazine and CHNO-tetrazine families respectively. Since these materials were first synthesized relatively recently, there is not a lot of published data on their performance. Additionally, to date, there is no known attempt to synthesize printable inks using these materials. Thus, BTATz and DAATO_{3.5} inks were synthesized for use

with a piezoelectric inkjet printing system. The solvent, binder, and solids loading were optimized for print quality. These inks were then analyzed using DSC/TGA to determine thermal stability and exotherm behavior. The results of the analysis showed that generally, the inks used are more thermally stable than the pure high nitrogen materials. Three additional studies were conducted to quantify the combustion performance of these inks.

The high nitrogen inks were also used to print lines for burning rate experiments. Burning rates versus the number of printed layers for both inks were determined using a high-speed camera. The results indicate that the DAATO_{3.5} samples generally burn two times faster than BTATz samples. Additionally, a confinement study was conducted on printed BTATz lines. The results indicated that confining the printed lines can increase the burning rate by an order of magnitude. It was theorized that this is likely due to a transition from diffusive to convective burning.

A closed pressure bomb study was used to determine the gas producing performance of these high nitrogen inks. A Parr cell was fitted with dynamic and static sensors to collect peak pressures and pressurization rates. Samples with varying volumes of each type of ink were confined and ignited within the Parr cell. The resulting data indicated that the BTATz ink was more effective than the DAATO_{3.5} ink in terms of maximum static pressures achieved as well as pressurization rates. A thermochemical modeling software and simplified model were employed to validate the experimental data. The software used was CHEETAH 7.0 which uses several idealized assumptions. The simplified model used assumptions to more closely reflect the experimental conditions. The experimental data closely followed the trends and values predicted by both models.

Finally, a 3D printed microthruster prototype was developed for use with the high nitrogen inks. The microthruster samples were loaded with varying volumes of each ink type. The thrust performance of the samples was analyzed using a microforce transducer. The peak thrust, total impulse, and specific impulse were determined for each sample. Microthrusters loaded with BTATz ink outperformed those loaded with DAATO_{3.5} in all three criteria. The specific impulse was higher for samples loaded with less propellant. While the peak thrust was highly variable for all microthruster configurations tested, the total impulse was generally more repeatable. In addition to single microthruster tests, a triangular shaped array of three chambers was prototyped. These

arrays were each tested to show that unintentional ignition of adjacent chambers does not occur when one chamber is ignited.

There are several avenues of future research to explore in the field of inkjet printing of EMs. For example, more parametric studies need to be conducted on how printing and ink formulation parameters affect final combustion performance to better understand how to optimize these systems. However, the work presented in this thesis provides a foundation for the use of HN EMs in printing systems. The studies performed show that this area of research is worth pursuing further and that the numerous applications are viable.

REFERENCES

- [1] A. K. Sikder and N. Sikder, "A review of advanced high performance, insensitive and thermally stable energetic materials emerging for military and space applications," *Journal of Hazardous Materials*, vol. 112, no. 1–2, pp. 1–15, Aug. 2004.
- [2] C. Rossi, S. Orioux, B. Larangot, T. Do Conto, and D. Estève, "Design, fabrication and modeling of solid propellant microrocket-application to micropropulsion," *Sensors and Actuators A: Physical*, vol. 99, no. 1–2, pp. 125–133, Apr. 2002.
- [3] D. Sundaram, V. Yang, and R. A. Yetter, "Metal-based nanoenergetic materials: Synthesis, properties, and applications," *Progress in Energy and Combustion Science*, vol. 61, pp. 293–365, Jul. 2017.
- [4] C. S. Staley, K. E. Raymond, R. Thiruvengadathan, S. J. Apperson, K. Gangopadhyay, S. M. Swaszek, R. J. Taylor, and S. Gangopadhyay, "Fast-Impulse Nanothermite Solid-Propellant Miniaturized Thrusters," *Journal of Propulsion and Power*, vol. 29, no. 6, pp. 1400–1409, Nov. 2013.
- [5] R. Shen, Y. Ye, C. Wang, C. Ru, and J. Dai, "Chemical Propulsion of Microthrusters," in *Nanomaterials in Rocket Propulsion Systems*, Elsevier, 2019, pp. 389–402.
- [6] C. Ru, F. Wang, J. Xu, J. Dai, Y. Shen, Y. Ye, P. Zhu, and R. Shen, "Superior performance of a MEMS-based solid propellant microthruster (SPM) array with nanothermites," *Microsystem Technologies*, vol. 23, no. 8, pp. 3161–3174, Aug. 2017.
- [7] J. Dai, F. Wang, C. Ru, J. Xu, C. Wang, W. Zhang, Y. Ye, and R. Shen, "Ammonium perchlorate as an effective additive for enhancing the combustion and propulsion performance of Al/CuO nanothermites," *The Journal of Physical Chemistry C*, vol. 122, no. 18, pp. 10240–10247, 2018.
- [8] A. K. Murray, T. Isik, V. Ortalan, I. E. Gunduz, S. F. Son, G. T.-C. Chiu, and J. F. Rhoads, "Two-component additive manufacturing of nanothermite structures via reactive inkjet printing," *Journal of Applied Physics*, vol. 122, no. 18, p. 184901, Nov. 2017.
- [9] A. S. Tappan, J. P. Ball, and J. W. Colovos, "Inkjet printing of energetic materials: Al/MoO₃ and Al/Bi₂O₃ thermite," in *Proc. 38th Int. Pyrotech. Seminar*, 2012, pp. 605–613.
- [10] R. R. Nellums, B. C. Terry, B. C. Tappan, S. F. Son, and L. J. Groven, "Effect of Solids Loading on Resonant Mixed Al-Bi₂O₃ Nanothermite Powders," *Propellants, Explosives, Pyrotechnics*, vol. 38, no. 5, pp. 605–610, 2013.
- [11] T. J. Fleck, "Additive Manufacturing of Energetic Materials and Its Uses in Various Applications," M.S.M.E., Purdue University, United States -- Indiana, 2017.

- [12] A. K. Murray, W. A. Novotny, T. J. Fleck, I. E. Gunduz, S. F. Son, G. T. -C. Chiu, and J. F. Rhoads, "Selectively-deposited energetic materials: A feasibility study of the piezoelectric inkjet printing of nanothermites," *Additive Manufacturing*, vol. 22, pp. 69–74, Aug. 2018.
- [13] E. R. Westphal, A. K. Murray, M. P. McConnell, T. J. Fleck, G. T.-C. Chiu, J. F. Rhoads, I. E. Gunduz, and S. F. Son, "The Effects of Confinement on the Fracturing Performance of Printed Nanothermites," *Propellants, Explosives, Pyrotechnics*, vol. 44, no. 1, pp. 47–54, Jan. 2019.
- [14] V. P. Sinditskii, V. Yu. Egorshv, G. F. Rudakov, A. V. Burzhava, S. A. Filatov, and L. D. Sang, "Thermal behavior and combustion mechanism of high-nitrogen energetic materials DHT and BTATz," *Thermochimica Acta*, vol. 535, pp. 48–57, May 2012.
- [15] V. P. Sinditskii, V. Y. Egorshv, G. F. Rudakov, S. A. Filatov, and A. V. Burzhava, "High-nitrogen energetic materials of 1, 2, 4, 5-tetrazine family: thermal and combustion behaviors," in *Chemical Rocket Propulsion*, Springer, 2017, pp. 89–125.
- [16] D. E. Chavez, M. A. Hiskey, M. H. Huynh, D. L. Naud, S. F. Son, and B. C. Tappan, "The combustion products of novel high-nitrogen energetic materials," *Journal of Pyrotechnics*, vol. 23, pp. 70, Jan. 2006.
- [17] D. E. Chavez and B. C. Tappan, "Synthesis and combustion characteristics of novel high-nitrogen materials," *International Journal of Energetic Materials and Chemical Propulsion*, vol. 12, no. 2, pp. 173–182, 2013.
- [18] S. F. Son, H. L. Berghout, C. A. Bolme, D. E. Chavez, D. Naud, and M. A. Hiskey, "Burn rate measurements of HMX, TATB, DHT, DAAF, and BTATz," *Proceedings of the Combustion Institute*, vol. 28, no. 1, pp. 919–924, 2000.
- [19] D. Naud, M. A. Hiskey, J. F. Kramer, R. L. Bishop, H. H. Harry, S. F. Son, and G. K. Sullivan, "High-nitrogen explosives," Los Alamos National Laboratory, 2002.
- [20] A. N. Ali, S. F. Son, M. A. Hiskey, and D. L. Naud, "Novel High Nitrogen Propellant Use in Solid Fuel Micropropulsion," *Journal of Propulsion and Power*, vol. 20, no. 1, pp. 120–126, Jan. 2004.
- [21] B. W. Asay, S. F. Son, J. R. Busse, and D. M. Oswald, "Ignition Characteristics of Metastable Intermolecular Composites," *Propellants, Explosives, Pyrotechnics*, vol. 29, no. 4, pp. 216–219, Aug. 2004.
- [22] K. Meeks, M. L. Pantoya, and C. Apblett, "Deposition and characterization of energetic thin films," *Combustion and Flame*, vol. 161, no. 4, pp. 1117–1124, Apr. 2014.
- [23] B. S. Bockmon, M. L. Pantoya, S. F. Son, B. W. Asay, and J. T. Mang, "Combustion velocities and propagation mechanisms of metastable interstitial composites," *Journal of Applied Physics*, vol. 98, no. 6, p. 064903, Sep. 2005.

- [24] A. Saikia, R. Sivabalan, B. G. Polke, G. M. Gore, A. Singh, A. S. Rao, and A. K. Sikder, "Synthesis and characterization of 3,6-bis(1H-1,2,3,4-tetrazol-5-ylamino)-1,2,4,5-tetrazine (BTATz): Novel high-nitrogen content insensitive high energy material," *Journal of Hazardous Materials*, vol. 170, no. 1, pp. 306–313, Oct. 2009.
- [25] K. M. Koczur, S. Mourdikoudis, L. Polavarapu, and S. E. Skrabalak, "Polyvinylpyrrolidone (PVP) in nanoparticle synthesis," *Dalton Trans.*, vol. 44, no. 41, pp. 17883–17905, Oct. 2015.
- [26] N. G. Tanikella, B. Wittbrodt, and J. M. Pearce, "Tensile strength of commercial polymer materials for fused filament fabrication 3D printing," *Additive Manufacturing*, vol. 15, pp. 40–47, May 2017.
- [27] K. L. Zhang, S. K. Chou, and S. S. Ang, "Development of a solid propellant microthruster with chamber and nozzle etched on a wafer surface," *Journal of Micromechanics and Microengineering*, vol. 14, no. 6, pp. 785–792, Jun. 2004.
- [28] S. Bastea, L. E. Fried, K. R. Glaeseman, W. M. Howard, I. F. W. Kuo, P. C. Souers, and P. A. Vitello, "Cheetah 7.0 thermochemical code," *Livermore (CA): Energetic Materials Center: Lawrence Livermore National Laboratory*, 2012.
- [29] S. J. Apperson, A. V. Bezmelnitsyn, R. Thiruvengadathan, K. Gangopadhyay, S. Gangopadhyay, W. A. Balas, P. E. Anderson, and S. M. Nicolich, "Characterization of Nanothermite Material for Solid-Fuel Microthruster Applications," *Journal of Propulsion and Power*, vol. 25, no. 5, pp. 1086–1091, Sep. 2009.
- [30] K. Sathyanathan, R. Lee, H. Chesser, C. Dubois, R. Stowe, R. Farinaccio, and S. Ringuette, "Solid Propellant Microthruster Design for Nanosatellite Applications," *Journal of Propulsion and Power*, vol. 27, no. 6, pp. 1288–1294, Nov. 2011.
- [31] X. Wu, P. Dong, Z. Li, S. Li, Q. Liu, C. Xu, and H. Wan, "Design, fabrication and characterization of a solid propellant micro-Thruster," in *2009 4th IEEE International Conference on Nano/Micro Engineered and Molecular Systems*, Shenzhen, China, 2009, pp. 476–479.